Signature of primordial non-Gaussianity of 3 type in the mass function and bias of dark matter haloes

Desjacques, V ; Seljak, U

Abstract: We explore the effect of a cubic correction gNL 3 on the mass function and bias of dark matter haloes extracted from a series of large N-body simulations and compare it to theoretical predictions. Such cubic terms can be motivated in scenarios like the curvaton model, in which a large cubic correction can be produced while simultaneously keeping the quadratic fNL 2 correction small. The deviation from the Gaussian halo mass function is in reasonable agreement with the theoretical predictions. The scale-dependent bias correction Δb (k,gNL) measured from the auto- and cross-power spectrum of haloes, is similar to the correction in fNL models, but the amplitude is lower than theoretical expectations. Using the compilation of LSS data in [A. Slosar , J. Cosmol. Astropart. Phys.1475-7516 08 (2008) 03110.1088/1475-7516/2008/08/031], we obtain for the first time a limit on gNL of -3.5×105<gNL<+8.2×105 (at 95% CL). This limit will improve with the future LSS data by 1-2 orders of magnitude, which should test many of the scenarios of this type.

DOI: https://doi.org/10.1103/PhysRevD.81.023006

Other titles: Signature of primordial non-Gaussianity of phi^3−*typeinthemassfunctionandbiasofdarkmatterhaloes*

Signature of primordial non-Gaussianity of ϕ^3-type in the mass function and bias of dark matter haloes

Vincent Desjacques[1] and Uroš Seljak[1,2,3]
[1] Institute for Theoretical Physics, University of Zürich, Winterthurerstrasse 190, CH-8057 Zürich, Switzerland
[2] Physics and Astronomy Department, University of California, and Lawrence Berkeley National Laboratory, Berkeley, California 94720, USA
[3] IEU, Ewha University, Seoul, S. Korea*

We explore the effect of a cubic correction $g_{\rm NL}\phi^3$ on the mass function and bias of dark matter haloes extracted from a series of large N-body simulations and compare it to theoretical predictions. Such cubic terms can be motivated in scenarios like the curvaton model, in which a large cubic correction can be produced while simultaneously keeping the quadratic $f_{\rm NL}\phi^2$ correction small. The deviation from the Gaussian halo mass function is in reasonable agreement with the theoretical predictions. The scale-dependent bias correction $\Delta b_\kappa(k, g_{\rm NL})$ measured from the auto- and cross-power spectrum of haloes, is similar to the correction in $f_{\rm NL}$ models, but the amplitude is lower than theoretical expectations. Using the compilation of LSS data in Slosar et al. [JCAP, **08**, 031 (2008)], we obtain for the first time a limit on $g_{\rm NL}$ of $-3.5\times10^5 < g_{\rm NL} < +8.2\times10^5$ (at 95% CL). This limit will improve with the future LSS data by 1-2 orders of magnitude, which should test many of the scenarios of this type.

PACS numbers: 98.65.-r, 98.80.Cq, 95.36.+x, 98.70.Vc

I. INTRODUCTION

In standard single field inflation, primordial curvature perturbations are produced by the inflaton field as it slowly rolls down its potential ([1, 2, 3, 4]). Most of these models predict a nearly scale-invariant spectrum of adiabatic curvature fluctuations in agreement with cosmological observations. In addition, very small deviations from Gaussianity are expected [5, 6, 7]. Therefore, any evidence for or against the detection of primordial non-Gaussianity would strongly constrain inflationary scenarios.

Non-Gaussianity can be produced by nonlinearities in the relation between the primordial curvature perturbation Φ (Here and henceforth, the usual Bardeen potential in matter-dominated era) and the inflaton field, interactions of scalar fields, a modified dispersion relation or a departure from the natural adiabatic vacuum state (see [8] for a review). Any non-Gaussianity that is generated outside the horizon induces a three-point function (or bispectrum) $B_\Phi(\mathbf{k}_1, \mathbf{k}_2, \mathbf{k}_3)$ that is peaked on squeezed triangles (i.e. $k_1 \ll k_2 \sim k_3$) for realistic values of the scalar spectral index. The resulting non-Gaussianity depends only on the local value $\Phi(\mathbf{x})$ of the Bardeen's curvature potential and can thus be conveniently parametrised up to third order by

$$\Phi(\mathbf{x}) = \phi(\mathbf{x}) + f_{\rm NL}\big[\phi^2(\mathbf{x}) - \langle\phi^2\rangle\big] + g_{\rm NL}\phi^3(\mathbf{x})\,, \quad (1)$$

where $\phi(\mathbf{x})$ is an isotropic Gaussian random field and $f_{\rm NL}$, $g_{\rm NL}$ are dimensionless, phenomenological parameters. While the quadratic term generates the irreducible three-point function or bispectrum at leading order, the cubic term does so for the irreducible four-point function or trispectrum. These statistics can be computed straightforwardly from a perturbative expansion of the homogeneous Robertson-Walker background [9, 10]. Convolved with the appropriate transfer function (e.g. the radiation transfer function for the CMB temperature anisotropy), they can be used to constrain the value of the coupling parameters $f_{\rm NL}$ and $g_{\rm NL}$. No significant detection of primordial non-Gaussianity has been reported from measurements of the three-point correlation function of the cosmic microwave background (CMB) anisotropies [11, 12, 13, 14, 15]. The tightest limits are $-4 < f_{\rm NL} < 80$ at 95% confidence level [14].

If $\mathcal{O}(f_{\rm NL}) \sim \mathcal{O}(g_{\rm NL})$ then the cubic correction should always be negligibly small compared to the quadratic one since curvature perturbations are typically $\mathcal{O}(10^{-5})$. However, this condition is not satisfied by some multifield inflationary models such as the curvaton scenario, in which a large $g_{\rm NL}$ and a small $f_{\rm NL}$ can be simultaneously produced. In this model, curvature perturbations are generated by an additional scalar field, the curvaton, whose energy density is negligible during inflation [16, 17, 18, 19]. Non-Gaussianity is generated by curvaton self-interactions which effectively contribute a non-quadratic term to the curvaton potential [20, 21, 22, 23, 24]. While the value and the sign of $g_{\rm NL}$ depend upon the exact form of the self-interaction term (which can dominate the mass term if the curvaton mass is small enough and the curvaton vacuum expectation value during inflation is large enough [25]), it is generically of magnitude $|g_{\rm NL}| \sim 10^4 - 10^5$ for realistic models in which the ratio of the energy density of the curvaton to the total energy density at time of decay is small. There are other realizations where one can have large $g_{\rm NL}$

*dvince@physik.uzh.ch; seljak@physik.uzh.ch

and small $f_{\rm NL}$ [26, 27]. In ekpyrotic and cyclic models, $f_{\rm NL}$ typically is of the order of a few tens while $g_{\rm NL}$ is of the order of a few thousand [28]. If $f_{\rm NL}$ were small, then the imprint of non-Gaussianity would be detected only in four-point statistics such as the CMB trispectrum [29, 30, 31]. Thus far, no observational limits have been set on $g_{\rm NL}$ by measuring the CMB trispectrum [32, 33]. Nevertheless, since the current bound $|f_{\rm NL}| \lesssim 100$ implies a relative contribution for the quadratic term of ~ 0.1 per cent, a third order coupling parameter $|g_{\rm NL}| \sim 10^6$ should also be consistent with the data.

Large-scale structures offer another venue to test for the presence of primordial non-Gaussianity. Deviation from Gaussianity can significantly affect the high mass end of the mass function [34, 35], the large-scale two-point correlation [36, 37], the bispectrum [38, 39, 40, 41] of dark matter haloes hosting the observed galaxies as well as void abundances [42, 43] and topological measures of the cosmic web [44, 45]. Recently, references [46, 47, 48] showed that the local quadratic coupling $f_{\rm NL}\phi^2$ induces a scale-dependent bias $\Delta b_\kappa(k, f_{\rm NL})$ in the large-scale power spectrum of biased tracers,

$$\Delta b_\kappa(k, f_{\rm NL}) = 3 f_{\rm NL}\big[b(M) - 1\big]\delta_{\rm c}\frac{\Omega_{\rm m}H_0^2}{k^2 T(k) D(z)}\ , \qquad (2)$$

where $b(M)$ is the linear bias parameter, H_0 is the Hubble parameter, $T(k)$ is the matter transfer function normalised to unity as $k \to 0$, $D(z)$ is the growth factor normalised to $(1+z)^{-1}$ in the matter era and $\delta_{\rm c} \sim 1.68$ is the present-day (linear) critical density threshold. Reference [48] applied Eq. (2) to constrain the value of $f_{\rm NL}$ using a compilation of large-scale structure data and found $-29 < f_{\rm NL} < +69$ at 95% confidence. These limits are comparable with those from the CMB, demonstrating the competitiveness of the method. Forthcoming all sky surveys should achieve constraints of the order of $f_{\rm NL} \sim 1$ [46, 49, 50, 51] and should be sensitive to a possible scale-dependence of $f_{\rm NL}$ [52]. On the numerical side however, while simulations of structure formation have confirmed the scaling $\Delta b_\kappa(k, f_{\rm NL})$ with k [46, 53, 54, 55], the exact amplitude of the non-Gaussian bias correction remains somewhat debatable.

All numerical studies to date have only implemented the quadratic term $f_{\rm NL}\phi^2$. The purpose of this work is to quantify the impact of the cubic term $g_{\rm NL}\phi^3$ on the mass function and bias of dark matter haloes extracted from cosmological simulations and assess the ability of forthcoming measurements of the large-scale bias of galaxies/quasars to constrain the size of a local cubic correction. This paper is organized as follows. We begin with a brief description of the N-body simulations and illustrate the extent to which the coupling $g_{\rm NL}\phi^3$ affects the matter power spectrum and the halo mass function (Sec. II). We pursue with the non-Gaussian halo bias (Sec. III), to which we derive analytically the scale-dependent and scale-independent contribution, Δb_κ and $\Delta b_{\rm I}$, and demonstrates the large suppression of the simulated Δb_κ relative to theory. We then place limits on the coupling parameter $g_{\rm NL}$ and forecast constraints from future large-scale surveys and CMB experiments (Sec. IV). We also show that our findings consistently apply to more general models with non-zero $f_{\rm NL}$ and $g_{\rm NL}$ (Sec. V). We conclude with a discussion of the results in Sec. VI.

II. THE NON-GAUSSIAN SIMULATIONS

A. Characteristics of the N-body runs

We utilize a series of large N-body simulations of the ΛCDM cosmology seeded with Gaussian and non-Gaussian initial conditions. The (dimensionless) power spectrum of the Gaussian part $\phi(\mathbf{x})$ of the Bardeen potential is the usual power-law $\Delta^2_\phi(k) \equiv k^3 P_\phi(k)/(2\pi^2) = A_\phi (k/k_0)^{n_s - 1}$. The non-Gaussianity is of the "local" form $\Phi = \phi + g_{\rm NL}\phi^3$. We adopt the standard (CMB) convention in which $\Phi(\mathbf{x})$ is primordial, and not extrapolated to present epoch. It is important to note that the local transformation is performed before multiplication by the matter transfer function. $T(k)$ is computed with CMBFAST [56] for the WMAP5 best-fitting parameters [13] : $h = 0.7$, $\Omega_{\rm m} = 0.279$, $\Omega_{\rm b} = 0.0462$, $n_s = 0.96$ and a normalisation of the Gaussian curvature perturbations $A_\phi = 7.96 \times 10^{-10}$ at the pivot point $k_0 = 0.02{\rm Mpc}^{-1}$. This yields a density fluctuations amplitude $\sigma_8 \approx 0.81$ when the initial conditions are Gaussian. Five sets of three 1024^3 simulations, each of which has $g_{\rm NL} = 0, \pm 10^6$, were run with the N-body code GADGET2 [57]. We used the same Gaussian random seed field ϕ in each set of runs so as to minimise the sampling variance. We also explored scenarios with non-zero $f_{\rm NL}$ and $g_{\rm NL}$ and ran 2 realisations for each of the non-Gaussian models characterized by $(f_{\rm NL}, g_{\rm NL}) = (\pm 100, -3 \times 10^5)$. In all cases, the box size is 1600 h^{-1}Mpc with a force resolution of 0.04 times the mean interparticle distance. The particle mass of these simulations thus is 3.0×10^{11} $\rm M_\odot/\mathit{h}$, enough to resolve haloes down to 10^{13} $\rm M_\odot/\mathit{h}$.

In the curvaton scenario, generic polynomial interaction terms of the form $\lambda m_\sigma^4 (\sigma/m_\sigma)^n$ (where λ is some coupling strength and m_σ is the curvaton mass) to the quadratic potential of the curvaton field σ yield $|g_{\rm NL}| \gg 1$ even when the non-linearity parameter $f_{\rm NL}$ is very small [21, 22]. One typically finds $|g_{\rm NL}| \sim \mathcal{O}(10^4) - \mathcal{O}(10^5)$ when $f_{\rm NL}$ varies in the range $-100 < f_{\rm NL} < 100$. For practical reasons however, the values of $g_{\rm NL}$ adopted in our simulations are about an order of magnitude larger so as to produce an effect strong enough to be unambiguously measured despite the small simulated volume. Furthermore, we have also considered positive and negative values of $g_{\rm NL}$ so as to assess the sensitivity of the non-Gaussian bias to the sign of the coupling parameter. The simulations with $(f_{\rm NL}, g_{\rm NL}) = (-100, -3 \times 10^5)$ may be seen as a particular realisation of the curvaton model in which the coupling constant λ is positive, and the non-quadratic term is very steep ($n \sim 5 - 10$) but contributes little to the total curvaton potential.

B. Properties of the initial density field

In order to ensure that the initial conditions are successfully generated, we measure at the redshift of our initial conditions, $z = 99$, the (normalized) skewness $S_3(R,z) = \langle\delta^3_{R,z}\rangle/\sigma^4$ and kurtosis $S_4(R,z) = (\langle\delta^4_{R,z}\rangle/ - 3\sigma^4)/\sigma^6$ of the density field $\delta_{R,z}$ smoothed with a (spherically symmetric) window function of characteristic radius R. We adopt a tophat filter throughout this paper. Note also that $\sigma(R,z)$ is the variance of smoothed density fluctuations at redshift z.

In the weakly nonlinear regime, the skewness and kurtosis of the density field may be written as the sum of a part generated by gravitational clustering and a part induced by primordial non-Gaussianity. For Zel'dovich initial conditions [58] and $\Omega_m(z) \approx 1$, the contribution generated by gravitational instabilities reads as [59, 60, 61, 62]

$$S_3^{\rm Zel}(R,z) = 4 - (n_{\rm eff}+3) \qquad (3)$$
$$S_4^{\rm Zel}(R,z) = \frac{272}{9} - \frac{50}{3}(n_{\rm eff}+3) + \frac{7}{3}(n_{\rm eff}+3)^2 \ ,$$

where $n_{\rm eff}(R)$ is the effective spectral index at the smoothing scale R,

$$n_{\rm eff}(R) \equiv -\frac{d\ln\sigma^2(R,z)}{d\ln R} - 3 \ . \qquad (4)$$

Note that the initial skewness and kurtosis given by the Zel'dovich approximation differs from the exact values predicted by perturbation theory, to which they asymptote in the limit $D(z) \to \infty$ [63]. In addition, the cubic coupling $g_{\rm NL}\phi^3$ induces a nonzero kurtosis $S_4^{\rm Pri}(R,z) \equiv g_{\rm NL}S_4^{(1)}(R,z)$ at leading order which can be computed analytically from the relation

$$\sigma^6 S_4^{(1)}(R,z) = 4!\left(\prod_{i=1}^{3}\int\frac{d^3k_i}{(2\pi)^3}\,\alpha_R(k_i,z)P_\phi(k_i)\right) \times \alpha_R\big(|\mathbf{k}_1+\cdots+\mathbf{k}_{n-1}|,z\big) \ , \qquad (5)$$

where

$$\alpha_R(k,z) = \frac{2}{3\Omega_{\rm m}H_0^2}D(z)k^2T(k)W_R(k) \qquad (6)$$

is evaluated at redshift z and $W_R(k)$ is the Fourier transform of the tophat function. When $f_{\rm NL} = 0$, primordial skewness is not generated at the first order and, therefore, may be neglected.

Fig. 1 displays the initial skewness (top panel) and kurtosis (bottom panel) obtained upon distributing the dark matter particles onto a regular 512^3 mesh (i.e. of cell size $\approx 3\ h^{-1}$Mpc) using the cloud-in-cell (CIC) interpolation scheme. Symbols represent the numerical results averaged over the realisations. Because $S_4^{\rm Zel}$ (which is the sole contribution to the kurtosis in the Gaussian case) varies considerably between the realisations, we only show the absolute difference $|S_4^{\rm Pri}|$ between the kurtosis in the non-Gaussian ($g_{\rm NL} = \pm 10^6$) and the Gaussian ($g_{\rm NL} = 0$) runs. As expected, the skewness is very similar among the Gaussian and non-Gaussian simulations. While S_3 in the simulations agrees well with the skewness induced by the Zel'dovich dynamics Eq. (3) (solid curve), it is gradually suppressed as the filtering radius R approaches the cell size, presumably because of the finite resolution which smoothes also the fluctuations. Note that, in the simulations with nonzero $g_{\rm NL}$ and $f_{\rm NL}$, there is a large primordial skewness which is of magnitude $|S_3^{\rm Pri}| \sim$ a few on scale $R \lesssim 50\ h^{-1}$Mpc, consistent with theory. As can also be seen, the absolute value of the primordial kurtosis increases sharply with R, in very good agreement with the theoretical prediction.

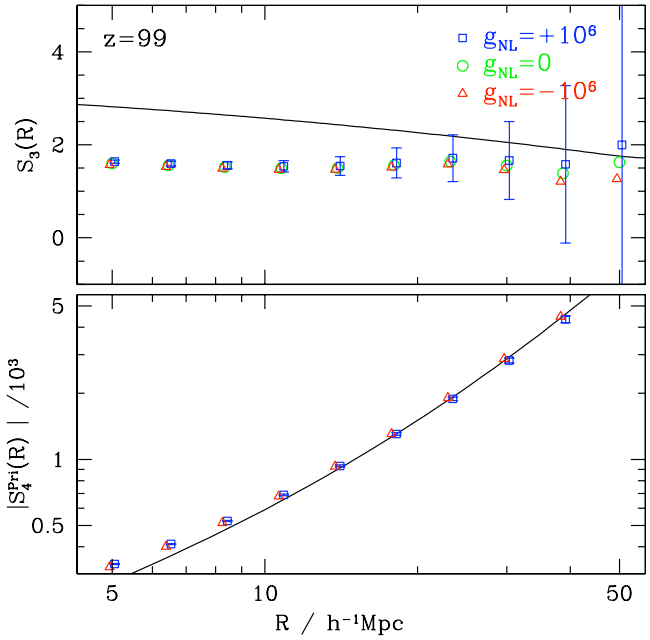

FIG. 1: Skewness and kurtosis of the initial ($z = 99$) density field as a function of smoothing radius. While the top panel shows the sum of the contributions arising from the Zel'dovich dynamics and from primordial non-Gaussianity, $S_3 = S_3^{\rm Zel} + S_3^{\rm Pri}$, the bottom panel only shows the absolute value of the primordial kurtosis, $|S_4^{\rm Pri}|$. Symbols represent the numerical results averaged over the realisations. They have been slightly shifted horizontally for clarity. Error bars show the scatter among the realisations for the models with $g_{\rm NL} = 10^6$. Solid lines indicate the theoretical expectations.

C. The matter power spectrum

Non-Gaussian corrections to the primordial curvature perturbation can renormalise the input power spectrum of fluctuations used to seed the simulations. Since our simulations implement its unrenormalised version $\Delta^2_\phi(k) = A_\phi(k/k_0)^{n_s-1}$, it is desirable to ascertain the

effect of the local coupling term on the simulated density power spectrum before discussing the halo mass function and bias. For $f_{\rm NL}$ models with $|f_{\rm NL}| \lesssim 100$, renormalisation effects are unlikely to be noticeable due to the limited dynamical range of current cosmological simulations [64]. As we will see shortly however, they can be significant in simulations of $g_{\rm NL}$ models with similar level of non-Gaussianity.

The cubic order term $g_{\rm NL}\phi^3$ renormalises the amplitude A_ϕ of the power spectrum of initial curvature perturbations to $A_\phi \to A_\phi + 6g_{\rm NL}\langle\phi^2\rangle$, where

$$\langle\phi^2\rangle = \int \frac{d^3k}{(2\pi)^3} P_\phi(k) \, . \tag{7}$$

For scale invariant initial conditions, $\langle\phi^2\rangle$ has a logarithmic divergence at large and small scales (see [64] for a more detailed discussion of perturbative corrections in non-Gaussian cosmologies). In practice, a low- and high-k cutoff are naturally provided by the finite box size and the resolution of the simulations. Therefore, the effective amplitude of density fluctuations in non-Gaussian simulations with cubic coupling is $\sigma_8 + \delta\sigma_8$ with

$$\begin{aligned} \delta\sigma_8 &= 3g_{\rm NL}\langle\phi^2\rangle \\ &= 3g_{\rm NL}\left(\frac{k_0}{k_{\rm min}}\right)^{1-n_s}\left[1-\left(\frac{k_{\rm min}}{k_{\rm max}}\right)^{1-n_s}\right]\frac{A_\phi}{1-n_s} \, . \end{aligned} \tag{8}$$

Recall that $k_0 = 0.02\ h{\rm Mpc}^{-1}$ is our choice of normalisation point, and $k_{\rm min}$ and $k_{\rm max}$ are the integration limits set by the fundamental mode and the Nyquist frequency of the periodic cubical box over which the initial conditions are generated. Equivalently,

$$\delta\sigma_8 = 3g_{\rm NL}\left(\frac{Lk_0}{2\pi}\right)^{1-n_s}\left[1-N^{n_s-1}\right]\frac{A_\phi}{1-n_s} \, , \tag{9}$$

where $N = 1024$ is the number of mesh points along one dimension. This result becomes $\delta\sigma_8 = 3g_{\rm NL}\ln(N)A_\phi$ in the scale-invariant limit $n_s \to 1$. For the cosmological setup considered here, the absolute deviation is

$$\delta\sigma_8 \approx 0.015\left(\frac{g_{\rm NL}}{10^6}\right) \, . \tag{10}$$

This correction is fairly large for the values of $g_{\rm NL}$ adopted here and, therefore, must be taken into account in the comparison between the theory and the simulations. As we will see below, this is especially important when studying the high mass tail of the halo mass function which is exponentially sensitive to the amplitude of density fluctuations.

The cubic coupling term $g_{\rm NL}\phi^3$ can also induce a scale-dependent correction to the matter power spectrum which can be quantified by the fractional change $\beta_{\rm m}(k, g_{\rm NL}) = P_{\rm mm}(k, g_{\rm NL})/P_{\rm mm}(k, g_{\rm NL} = 0) - 1$. In Fig. 2, symbols show the result of measuring $\beta_{\rm m}(k, g_{\rm NL})$ from the snapshots at $z = 0$ and 2 after correction of the normalisation shift $|2\delta\sigma_8/\sigma_8| = 0.037$. There is some evidence for a scale-dependent correction at wavenumber $k \gtrsim 0.1\ h{\rm Mpc}^{-1}$ but the resulting deviation is broadly consistent with zero. We will thus neglect $\beta_{\rm m}(k, g_{\rm NL})$ henceforth.

D. The halo multiplicity function

Haloes were identified using the MPI parallelised version of the AHF halo finder [65] which is based on the spherical overdensity (SO) finder developed by [66]. The main reason for using a SO finder is that it is more closely connected to the predictions of the spherical collapse model, on which most of the analytic formulae presented in this paper are based. Namely, the virial mass M of a halo is defined by the radius at which the inner overdensity exceeds $\Delta_{\rm vir}(z)$ times the background density $\bar\rho(z)$ [67, 68]. The value of the overdensity threshold $\Delta_{\rm vir}(z)$ is obtained from the collapse of a spherical tophat perturbation and has a dependence on redshift through the matter density $\Omega_m(z)$ [69, 70]. We discard poorly resolved haloes and only study those containing at least 34 particles or, equivalently, with a mass larger than $M = 10^{13}\ {\rm M}_\odot/h$.

Analytic arguments based on the Press-Schechter theory [71, 72] predict that the halo mass function $n(M, z)$ is entirely specified by the distribution $\nu f(\nu)$ of first-crossings, or multiplicity function

$$\nu f(\nu) = M^2\,\frac{n(M,z)}{\bar\rho}\frac{d\ln M}{d\ln\nu} \, . \tag{11}$$

The peak height $\nu(M, z) = \delta_{\rm c}(z)/\sigma(M)$ is the typical amplitude of fluctuations that produce haloes of mass M by redshift z. Here and henceforth, $\sigma(M)$ denotes the variance of the density field δ_M smoothed on mass scale $M \propto R^3$ and linearly extrapolated to present epoch, whereas $\delta_{\rm c}(z) \approx 1.68D(0)/D(z)$ is the critical linear overdensity for (spherical) collapse at redshift z.

Despite the lack of a compelling theoretical description of the multiplicity function for Gaussian initial conditions, the fractional deviation from Gaussianity can be modelled accurately using the Press-Schechter formalism. In this approach, the halo mass function $n(M, z)$ is related to the probability $P(> \delta_{\rm c}, M)$ that a region of mass M exceeds the critical density for collapse $\delta_{\rm c}(z)$ through the relation $n(M, z) = -2\,(\bar\rho/M)\,dP/dM$. The non-Gaussian fractional correction to the multiplicity function then is $R(\nu, g_{\rm NL}) \equiv f(\nu, g_{\rm NL})/f(\nu, 0) = (dP/dM)(> \delta_{\rm c}, M, g_{\rm NL})/(dP/dM)(> \delta_{\rm c}, M, 0)$. The level excursion probability $P(> \delta_{\rm c}, M, g_{\rm NL})$ can be computed once the probability distribution function (PDF) of the smoothed density field δ_M, $P(\delta_M)$, is known. Here, we will consider the simple extensions proposed by [73] and [74], in which $P(\delta_M)$ is generically expressed as the inverse transform of a cumulant generating function. Both extensions have been shown to give reasonable agreement with numerical simulations of non-Gaussian cosmologies [53, 55, 75].

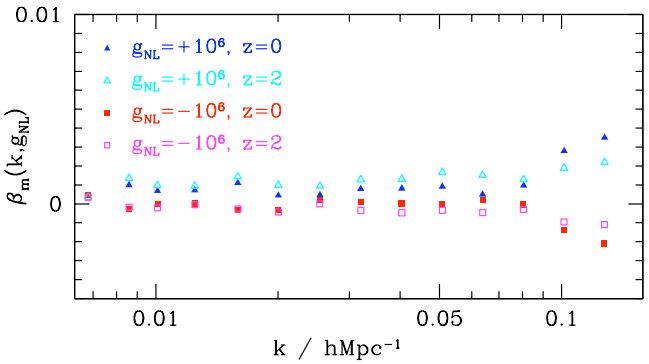

FIG. 2: Non-Gaussian fractional correction $\beta_{\rm m}(k, g_{\rm NL}) = P_{\rm mm}(k, g_{\rm NL})/P_{\rm mm}(k, 0) - 1$ to the matter power spectrum after subtracting a scale-independent normalisation shift $6g_{\rm NL}\langle\phi^2\rangle$ induced by the cubic coupling $g_{\rm NL}\phi^3$.

In [73], the saddle-point technique is applied directly to $P(\delta_M)$. The resulting Edgeworth expansion is then used to obtain $P(>\delta_{\rm c}, M, g_{\rm NL})$. For $f_{\rm NL}$ non-Gaussianity, reference [53] found that the resulting non-Gaussian mass function agrees well with the simulations. For $g_{\rm NL}$ non-Gaussianity, neglecting cumulants other than the kurtosis $S_4^{\rm Pri}(M)$ (Hereafter, we drop the superscript for conciseness) and truncating the series expansion at $S_4(M)$, the non-Gaussian fractional correction reads

$$R_{\rm LV}(\nu, g_{\rm NL}) \approx \left\{1 + \frac{1}{4!}\sigma^2 S_4\left(\nu^4 - 4\nu^2 - 3\right) - \frac{1}{4!}\sigma^2\frac{dS_4}{d\ln\nu}\left(\nu^2 - 3\right)\right\}\exp\left[\nu^2\delta\sigma_8\right] \quad (12)$$

$$= \left\{1 + \frac{1}{4!}\sigma^2 S_4\left(\nu^4 - 6\nu^2 + 3\right) - \frac{1}{4!}\frac{d(\sigma^2 S_4)}{d\ln\nu}\left(\nu^2 - 3\right)\right\}\exp\left[\nu^2\delta\sigma_8\right] \quad (13)$$

after integration over regions above $\delta_{\rm c}(z)$. Note that we have omitted writing the redshift dependence explicitly. Strictly speaking however, $R(\nu, g_{\rm NL})$ depends distinctly upon the variables M (or ν) *and* z due to the presence of $\sigma^2 S_4(M)$. Our notation is motivated by the fact that the measured non-Gaussian correction, as plotted in Fig.4, appears to depend mostly on the peak height. The exponential factor in the right-hand side is the correction induced by the renormalisation of the amplitude of linear density fluctuations, Eq. (10). For consistency, we have also used the Press-Schechter multiplicity function to derive this last term although a Sheth-Tormen mass function [76] may be more appropriate.

In [74], it is the level excursion probability $P(>\delta_{\rm c}, M)$ that is calculated within the saddle-point approximation. Including only a cubic coupling $g_{\rm NL}\phi^3$ and truncating the resulting expression at the kurtosis, we find

$$P(>\delta_{\rm c}, M, g_{\rm NL}) \approx \frac{1}{\sqrt{2\pi}}\frac{\sigma}{\delta_{\rm c}}\left(1 + 3g_{\rm NL}\sigma^2\langle\phi^2\rangle - \frac{S_4}{12}\sigma^2\delta_{\rm c}^2\right) \times \exp\left\{-\frac{\delta_{\rm c}^2}{2\sigma^2}\left[1 - 6g_{\rm NL}\langle\phi^2\rangle - \frac{S_4}{12}\delta_{\rm c}^2\right]\right\} \quad (14)$$

at first order in $g_{\rm NL}$. Note that we have already included the renormalisation of the fluctuation amplitude. For rare events, $\sigma \ll 1$ and the first parenthesis in the right-hand side can be neglected. To ensure that the resulting mass function is properly normalised, we follow [77] and use

$$\nu_\star f(\nu_\star) = M^2\,\frac{n(M, z, g_{\rm NL})}{\bar\rho}\frac{d\ln M}{d\ln\nu_\star}\,. \quad (15)$$

for the non-Gaussian mass function, where $\nu_\star = \delta_\star/\sigma$, $\delta_\star = \delta_{\rm c}\sqrt{1 - 2\delta\sigma_8 - S_4\delta_{\rm c}^2/12}$ [1] and f is the same multiplicity function as in the Gaussian case. Taking the derivative of the level excursion probability then gives

$$\frac{(dP/dM)(>\delta_{\rm c}, M, g_{\rm NL})}{(dP/dM)(>\delta_{\rm c}, M, 0)} \approx \exp\left[\frac{S_4\delta_{\rm c}^4}{4!\sigma^2} + \nu^2\delta\sigma_8\right] \times \left(\frac{\delta_\star}{\delta_{\rm c}} + \frac{1}{4!}\frac{\delta_{\rm c}^3}{\delta_\star}\frac{dS_4}{d\ln\sigma}\right)\,. \quad (16)$$

The fractional change in the multiplicity function eventually reads as

$$R_{\rm MVJ}(\nu, g_{\rm NL}) \approx \exp\left[\frac{\nu^4}{4!}\sigma^2 S_4 + \nu^2\delta\sigma_8\right] \times \left\{1 - \frac{\nu^2}{8}\sigma^2 S_4 - \frac{\nu^2}{4!}\frac{d(\sigma^2 S_4)}{d\ln\nu}\right\} \quad (17)$$

after expanding $\delta_\star$ at the first order and ignoring the shift in the normalisation amplitude, i.e. $\delta_\star^{\pm1} \approx 1 \mp S_4\delta_{\rm c}^2/24$. In the limit $\sigma^2 S_4 \ll 1$ and $\nu \gg 1$, the two theoretical expectations reduce to $1 + \nu^4\sigma^2 S_4/24$. However, they differ in the coefficient of the $\nu^2\sigma^2 S_4$ term, which is $-1/4$ and $-1/8$ for the LV and MVJ formula, respectively. There-

[1] In local $f_{\rm NL}$ models, this formula only involves the skewness S_3. As it is incorrectly quoted in some of the literature on non-Gaussian halo mass functions, let us write down its explicit expression:

$$R_{\rm MVJ}(\nu, f_{\rm NL}) = \exp\left[\frac{S_3\delta_{\rm c}^3}{6\sigma^2}\right]\left[\frac{\delta_{\rm c}^2}{6\delta_\star}\frac{dS_3}{d\ln\sigma} + \frac{\delta_\star}{\delta_{\rm c}}\right]\,,$$

or, in terms of the peak height $\nu = \delta_{\rm c}/\sigma$,

$$R_{\rm MVJ}(\nu, f_{\rm NL}) \approx \exp\left[\frac{\nu^3}{6}\sigma S_3\right]\left[1 - \frac{\nu}{3}\sigma S_3 - \frac{\nu}{6}\frac{d(\sigma S_3)}{d\ln\nu}\right]\,,$$

after expanding $\delta_\star = \sqrt{1 - S_3\delta_{\rm c}/3}$ at the first order.

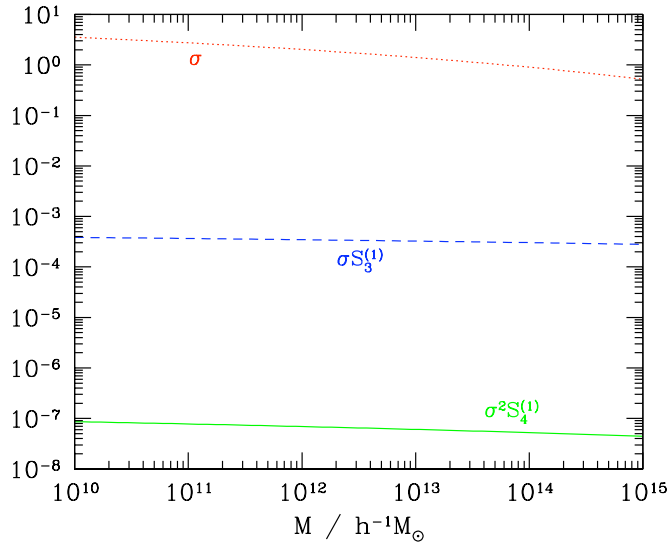

FIG. 3: Variance σ (dotted), skewness $\sigma S_3^{(1)}$ (dashed) and kurtosis $\sigma^2 S_4^{(1)}$ (solid) of the smoothed linear density field δ_M as a function of mass scale M.

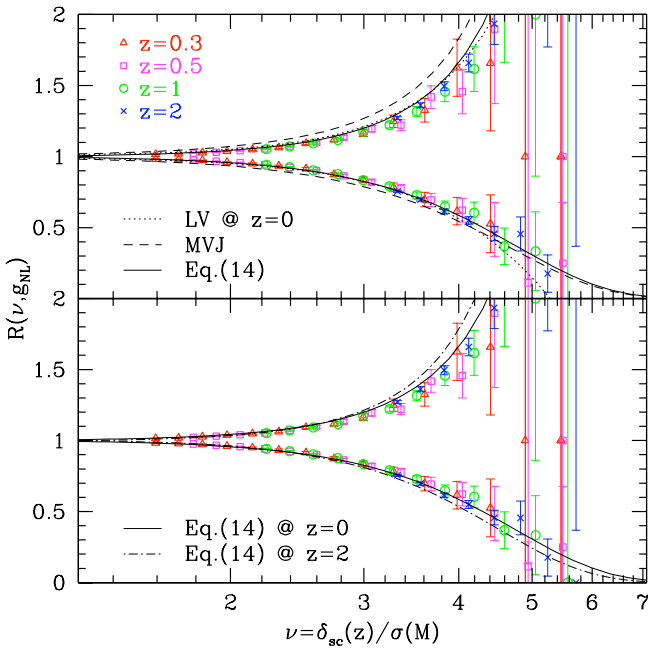

FIG. 4: *Top panel*: Fractional correction to the Gaussian multiplicity function of dark matter haloes as a function of the peak height $\nu(M,z)$ for a coupling parameter $g_{\rm NL} = \pm 10^6$. The dotted, dashed and solid curves show the theoretical predictions eqs. (13), (17) and (18) at $z = 0$, respectively. Error bars denote Poisson errors. For illustration, $M = 10^{15}$ M$_\odot/h$ corresponds to $\nu = 3.2$, 5.2, 7.7 at redshift $z = 0$, 1 and 2, respectively. Similarly, $M = 10^{14}$ M$_\odot/h$ and 10^{13} M$_\odot/h$ correspond to $\nu = 1.9$, 3, 4.5 and 1.2, 1.9, 2.9 respectively. *Bottom panel*: a comparison with equation (18) evaluated at $z = 0$ and 2.

fore, we shall also consider the approximation

$$R(\nu, g_{\rm NL}) = \exp\left[\frac{\nu^4}{4!}\sigma^2 S_4 + \nu^2 \delta\sigma_8\right] \times \left\{1 - \frac{\nu^2}{4}\sigma^2 S_4 - \frac{\nu^2}{4!}\frac{d(\sigma^2 S_4)}{d\ln\nu}\right\}, \quad (18)$$

which is designed to match better the Edgeworth expansion of [73] when the peak height is $\nu \sim 1$.

Calculating the fractional change in the mass function requires knowledge of the kurtosis $S_4(M) \equiv g_{\rm NL} S_4^{(1)}(M)$ of the smoothed density field δ_M, which we compute analytically using the general formula (valid for $n \geq 3$)

$$\sigma^{2n-2} S_n^{(1)}(M) = n! \left(\prod_{i=1}^{n-1} \int \frac{d^3 k_i}{(2\pi)^3}\, \alpha_M(k_i) P_\phi(k_i)\right) \times \alpha_M\left(|\mathbf{k}_1 + \cdots + \mathbf{k}_{n-1}|\right), \quad (19)$$

where $\alpha_M(k) \equiv \alpha_R(k, z = 0)$ in what follows. Over the mass range probed by our simulations, $10^{13} \lesssim M \lesssim 5 \times 10^{15}$ M$_\odot/h$, the normalised kurtosis $\sigma^2 S_4^{(1)}(M)$ is a monotonic decreasing function of M that varies in the narrow range $\sim 4-6\times10^{-7}$ for the top-hat filter assumed here (see Fig. 3). Note also that the $\sigma^2 S_4$ term dominates the total contribution to the non-Gaussian correction eqs. (13), (17) and (18) when the peak height is $\nu \gtrsim 2$ (One finds $|d(\sigma^2 S_4)/d\ln\nu| \lesssim 0.1\sigma^2 S_4$).

The fractional correction is plotted in Fig. 4 for the haloes extracted from the simulations at redshift $z = 0.3$, 0.5, 1 and 2. In the top panel, the data are compared to the theoretical predictions eqs. (13), (17) and (18) evaluated at $z = 0$. As we can see, the level of non-Gaussianity in the halo multiplicity function is consistent with the theory. Our approximation (18) performs equally well regardless of the sign of $g_{\rm NL}$. It agrees better with the measurements than the formulae of [74] which significantly overestimates the data for $g_{\rm NL} = 10^6$, and than that of [73] which is not always positive definite for $g_{\rm NL} = -10^6$. The bottom panel shows that the discrepancy somewhat worsens at higher redshift, especially in the case $g_{\rm NL} = 10^6$. However, it is possible the agreement may be improved by adding higher order powers of $\sigma^2 S_4$ and higher order cumulants.

To conclude this section, one should keep in mind that all these extensions are based on Press-Schechter and, therefore, provide a bad fit to the Gaussian mass function of haloes. In this respect, excursion set approaches may be more promising since they seem to reproduce both the Gaussian halo counts and the dependence on $f_{\rm NL}$ [78, 79].

III. THE NON-GAUSSIAN BIAS SHIFT

A. Theoretical considerations

In order to calculate the scale-dependent bias correction induced by the $g_{\rm NL}$ coupling term to the correlation of haloes of mass M collapsing at redshift z, we follow [47] and consider the two-point correlation $\xi_{\rm hh}(\mathbf{r})$ of regions of the smoothed density field δ_M above a threshold $\delta_c(z) = \nu(z)\sigma$. The two-point correlation function of this level excursion set, which was originally derived by [37], can be expressed in the high threshold approximation as

$$\xi_{\rm hh}(\mathbf{r}) = -1 + \exp\left\{ \sum_{n=2}^{\infty} \sum_{j=1}^{n-1} \frac{\nu^n \sigma^{-n}}{j!(n-j)!} \times \xi^{(n)}\left(\begin{array}{cc} \mathbf{x}_1, \cdots, \mathbf{x}_1, & \mathbf{x}_2, \cdots, \mathbf{x}_2 \\ j \text{ times} & (n-j) \text{ times} \end{array} \right) \right\} , \tag{20}$$

where $\mathbf{r} = \mathbf{x}_1 - \mathbf{x}_2$. For the non-Gaussian model considered here, the leading-order correction induced by non-zero three-point and four-point correlations of the density field reads

$$\Delta\xi_{\rm hh} = \frac{\nu^3}{\sigma^3}\xi^{(3)}(\mathbf{x}_1, \mathbf{x}_1, \mathbf{x}_2) + \frac{\nu^4}{\sigma^4}\left[\frac{1}{3}\xi^{(4)}(\mathbf{x}_1, \mathbf{x}_1, \mathbf{x}_1, \mathbf{x}_2) + \frac{1}{4}\xi^{(4)}(\mathbf{x}_1, \mathbf{x}_1, \mathbf{x}_2, \mathbf{x}_2) \right] . \tag{21}$$

The non-Gaussian correction $\Delta P_{\rm hh}$ to the power spectrum of biased tracers is obtained by Fourier transforming this expression.

In the case $f_{\rm NL} = 0$ and $g_{\rm NL} \neq 0$, only the four-point functions contribute at first order. It should also be noted that, at linear order, $\xi^{(2)}(\mathbf{x}_1, \mathbf{x}_2)$ amounts to a renormalisation of the linear bias and, therefore, does not contribute to the scale-dependent correction. Details of the calculation can be found in Appendix A. In short, the non-Gaussian correction $\Delta P_{\rm hh}$ in the limit of long wavelength $k \ll 1$ is given by the Fourier transform of $\nu^4\xi^{(4)}(\mathbf{x}_1, \mathbf{x}_1, \mathbf{x}_2, \mathbf{x}_2)/3\sigma^4$,

$$\begin{aligned} \Delta P_{\rm hh}(k) &= g_{\rm NL}\nu^4\, S_3^{(1)}(M)\alpha_M(k)P_\phi(k) \\ &= g_{\rm NL} b_{\rm L}^2(z)\delta_c^2(z)\, S_3^{(1)}(M)\alpha_M(k)P_\phi(k) , \end{aligned} \tag{22}$$

where we have used $b_{\rm L}(z) = \nu^2/\delta_c(z)$ as is appropriate for high density peaks. The smoothing window that appears in $\alpha_M(k)$ effectively makes little difference because we are considering the limit where k^{-1} is much larger than the smoothing radius, so we will omit it in the following. For small non-Gaussianity, we can also write $\Delta P_{\rm hh} \approx 2b_{\rm L}\Delta b_\kappa P_\delta(k)$ where $P_\delta(k) = \alpha_M^2 P_\phi(k)$ is the power spectrum of the smoothed density field. The scale-dependent bias correction $\Delta b_\kappa(k, g_{\rm NL})$ can eventually be recast into the form

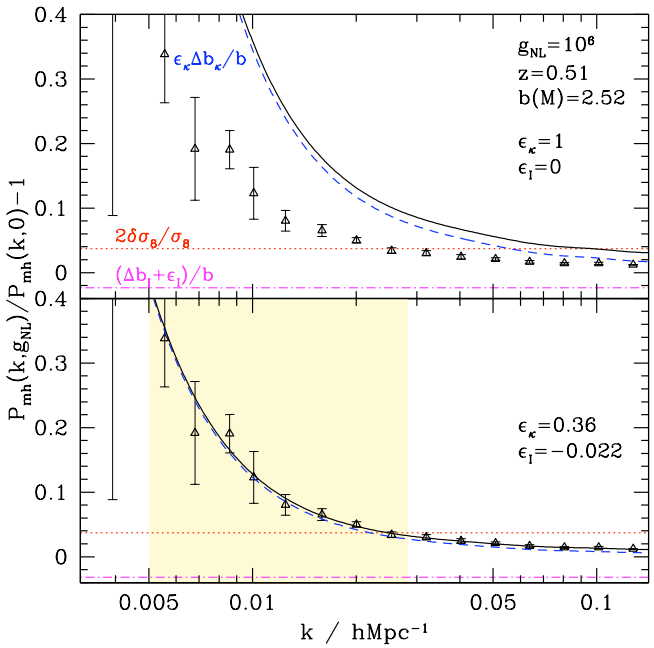

FIG. 5: *Top panel* : Non-Gaussian bias correction computed from the halo-matter power spectrum of haloes of mass $M > 2 \times 10^{13}\ {\rm M}_\odot/h$ extracted from the snapshot at $z = 0.5$ (filled symbols). The solid curve represents $P_{\rm mh}(k, g_{\rm NL})/P_{\rm mh}(k, 0) - 1$ with a non-Gaussian bias shift $\Delta b(k, g_{\rm NL})$ given by Eq. (26). The dashed, dotted and dotted-dashed curves show three separate contributions that arise at first order in $g_{\rm NL}$. *Bottom panel* : $\Delta b(k, g_{\rm NL})$ is replaced by the theoretical model Eq. (27). The shaded region indicates the data points used to fit the parameters ϵ_κ and $\epsilon_{\rm I}$. Error bars indicate the scatter among 5 realisations.

$$\begin{aligned} \Delta b_\kappa(k, g_{\rm NL}) &= \frac{1}{2} g_{\rm NL} b_{\rm L}(z)\delta_c^2(z)\, S_3^{(1)}(M)\alpha_M^{-1}(k) \\ &= \frac{3}{4} g_{\rm NL} b_{\rm L}(z)\delta_c^2(0)\frac{D(0)}{D(z)^2}\, S_3^{(1)}(M)\frac{\Omega_{\rm m}H_0^2}{k^2 T(k)} \\ &= \frac{1}{4} g_{\rm NL}\delta_c(z)\, S_3^{(1)}(M)\, \Delta b_\kappa(k, f_{\rm NL} = 1) , \end{aligned} \tag{23}$$

where $\Delta b_\kappa(k, f_{\rm NL})$ is the scale-independent bias induced by the quadratic coupling $f_{\rm NL}\phi^2$, Eq. (2). We have also assumed the Eulerian bias prescription $b(M) = 1 + b_{\rm L}(M)$.

The change in the mean number density of haloes also creates a scale-independent shift which we denote by $\Delta b_{\rm I}(g_{\rm NL})$. As shown in [53] for $f_{\rm NL}$ models, the inclusion of this correction noticeably improves the agreement with the simulations at wavenumber $k \lesssim 0.1\ h{\rm Mpc}^{-1}$. Using a peak-background split and considering the limit of small

non-Gaussianity, this contribution reads

$$\Delta b_{\rm I}(g_{\rm NL}) = -\frac{1}{\sigma}\frac{\partial}{\partial\nu}\ln\left[R(\nu,g_{\rm NL})\right] \approx -\frac{1}{\sigma}\left[\frac{1}{3!}\left(\nu^3-3\nu\right)\sigma^2 S_4 + 2\nu\delta\sigma_8 + \frac{1}{4!}\left(\nu^3-8\nu\right)\frac{d(\sigma^2S_4)}{d\ln\nu} - \frac{\nu}{4!}\frac{d^2(\sigma^2S_4)}{d\ln\nu^2}\right] \quad (24)$$

after truncating $\Delta b_{\rm I}$ at first order in $g_{\rm NL}$ This approximation should perform reasonably well for moderate values of the peak height, $\nu \lesssim 4$, for which the fractional change in the mass function, equation (18), matches well the numerical data. It is worth noticing that $\Delta b_{\rm I}(g_{\rm NL})$ has a sign opposite to that of $g_{\rm NL}$ because the bias decreases when the mass function goes up. $\Delta b_{\rm I}(g_{\rm NL})$ also includes a correction induced by the renormalisation of σ_8. In practice, we estimate $\Delta b_{\rm I}(g_{\rm NL})$ for a given halo sample by evaluating $\sigma^2 S_4$ and ν at the scale corresponding to the average halo mass $\bar{M}$ of the sample, as it is unclear to which extent $R(\nu, g_{\rm NL})$ agrees with the data in the limit $M \gg M_\star$.

B. Comparison with the simulations

To assess the effect of primordial non-Gaussianity on the halo bias, we will consider the ratios

$$\frac{P_{\rm mh}(k,g_{\rm NL})}{P_{\rm mh}(k,0)} - 1 = \frac{\Delta b(k,g_{\rm NL})}{b(M)} + 2\frac{\delta\sigma_8}{\sigma_8} \quad (25)$$
$$\frac{P_{\rm hh}(k,g_{\rm NL})}{P_{\rm hh}(k,0)} - 1 = \left(1+\frac{\Delta b(k,g_{\rm NL})}{b(M)}\right)^2 + 2\frac{\delta\sigma_8}{\sigma_8} - 1\,,$$

where $\Delta b(k, g_{\rm NL})$ is generally the sum of a scale-dependent and a scale-independent term. One should bear in mind that the scale-independent shift $2\delta\sigma_8/\sigma_8$ arises from the matter power spectrum and, therefore, is distinct from the term $-2\nu\delta\sigma_8/\sigma$ appearing in $\Delta b_{\rm I}$. Following [53], we shall also quantify the departure from the theoretical scaling as a function of wavemode amplitude with the ratio $\Delta b^s/\Delta b^t$, where Δb^s is the non-Gaussian bias correction measured from the simulation and Δb^t is Eq. (27).

We interpolate the dark matter particles and halo centres onto a regular cubical mesh. The resulting dark matter and halo fluctuation fields are then Fourier transformed to yield the matter-matter, halo-matter and halo-halo power spectra $P_{\rm mm}(k)$, $P_{\rm mh}(k)$ and $P_{\rm hh}(k)$, respectively. These power spectra are measured for a range of halo masses and redshifts, covering the relevant range of statistical properties corresponding to the available data sets of galaxy or quasar populations with different luminosities and bias. Note that these quantities are computed on a 512^3 grid, whose Nyquist wavenumber is sufficiently large ($\approx 1\ h{\rm Mpc}^{-1}$) to allow for an accurate measurement of the power in wavemodes of amplitude $k \lesssim 0.1\ h{\rm Mpc}^{-1}$. The halo power spectrum is corrected for the shot-noise due to the discrete nature of dark matter haloes, which we assume to be the standard Poisson term $1/\bar{n}_{\rm h}$. This discreteness correction is negligible for $P_{\rm mm}(k)$ due to the large number of dark matter particles. Yet another important quantity is the linear halo bias $b(M)$ which must be measured accurately from the Gaussian simulations as it controls the magnitude of the scale-dependent shift. Here, we shall use the ratio $P_{\rm mh}(k)/P_{\rm mm}(k)$ as a proxy for the halo bias since it is less sensitive to shot-noise.

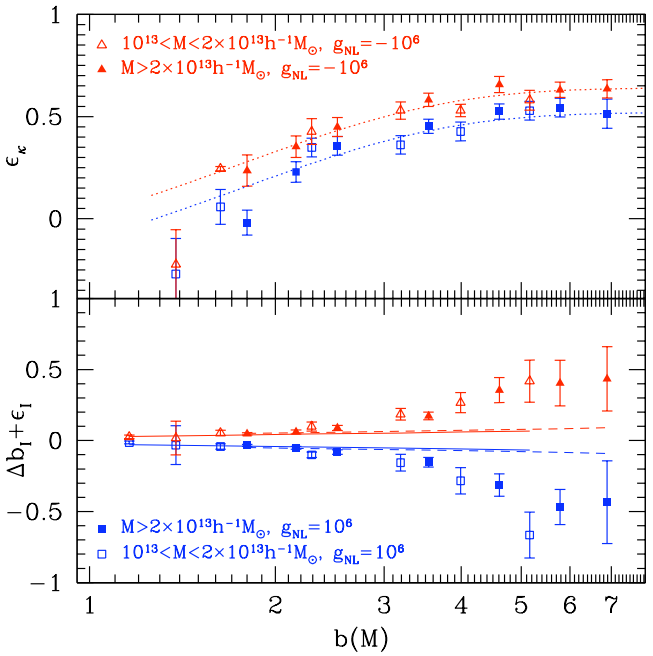

FIG. 6: Best-fitting ϵ_κ and $\Delta b_{\rm I} + \epsilon_{\rm I}$ as a function of halo bias and $g_{\rm NL} = \pm 10^6$, for two different mass cuts as indicated in the Figure. In the top panel, the dotted curve is our best fit to $\epsilon_\kappa(b, g_{\rm NL})$. In the bottom panel, the solid and dashed lines show the scale-independent shift $\Delta b_{\rm I}$ predicted by a peak-background split, Eq. (24), for the low and high mass samples, respectively.

1. *An effective non-Gaussian bias correction*

Summarizing the analytical considerations of Sec. III A, non-Gaussianity of the $g_{\rm NL}$ type add a correction $\Delta b(k, g_{\rm NL})$ to the bias $b(k)$ of dark matter haloes which is at leading order

$$\Delta b(k,g_{\rm NL}) = \Delta b_\kappa(k,g_{\rm NL}) + \Delta b_{\rm I}(g_{\rm NL})\,, \quad (26)$$

We found, however, that this theoretical expectation significantly overestimates the magnitude of the non-Gaussian bias shift measured from the simulations. This is exemplified in the top panel of Fig. 5, where $P_{\rm mh}(k,g_{\rm NL})/P_{\rm mh}(k,0) - 1$ is plotted for haloes of mass $M > 2\times10^{13}\ {\rm M}_\odot/h$ identified at $z = 0.5$. Clearly, the

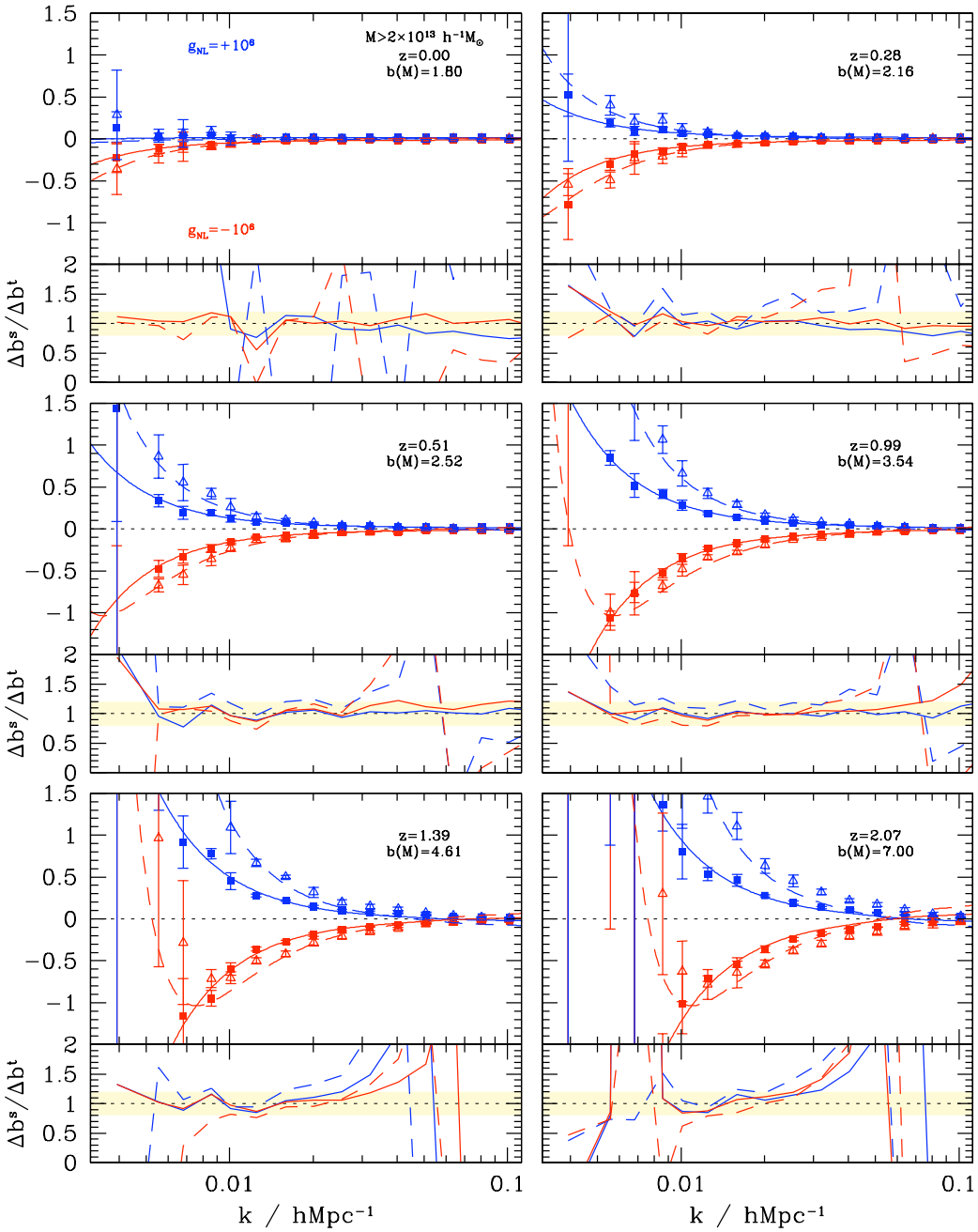

FIG. 7: Non-Gaussian bias correction measured in the simulation outputs at redshift $0 < z < 2$ for haloes of mass $M > 2 \times 10^{13}$ $\mathrm{M}_\odot/h$. In each panel, the upper plot shows the ratio $P_{\rm hh}(k, g_{\rm NL})/P_{\rm hh}(k, 0) - 1$ (dashed curves, empty symbols) and $P_{\rm mh}(k, g_{\rm NL})/P_{\rm mh}(k, 0) - 1$ (solid curves, filled symbols). The error bars represent the scatter among 5 realisations. The respective output redshift and linear halo bias are also quoted. The bottom of each panel displays the departure from the theoretical prediction, $\Delta b^s/\Delta b^t$. The shaded area indicates the domain where the deviation is less than 20 per cent. The parameters ϵ_κ and $\epsilon_{\rm I}$ are fitted individually to each sample. For illustration, ϵ_κ takes the best-fit values 0.06 and 0.60 for the lowest and highest biased samples, respectively.

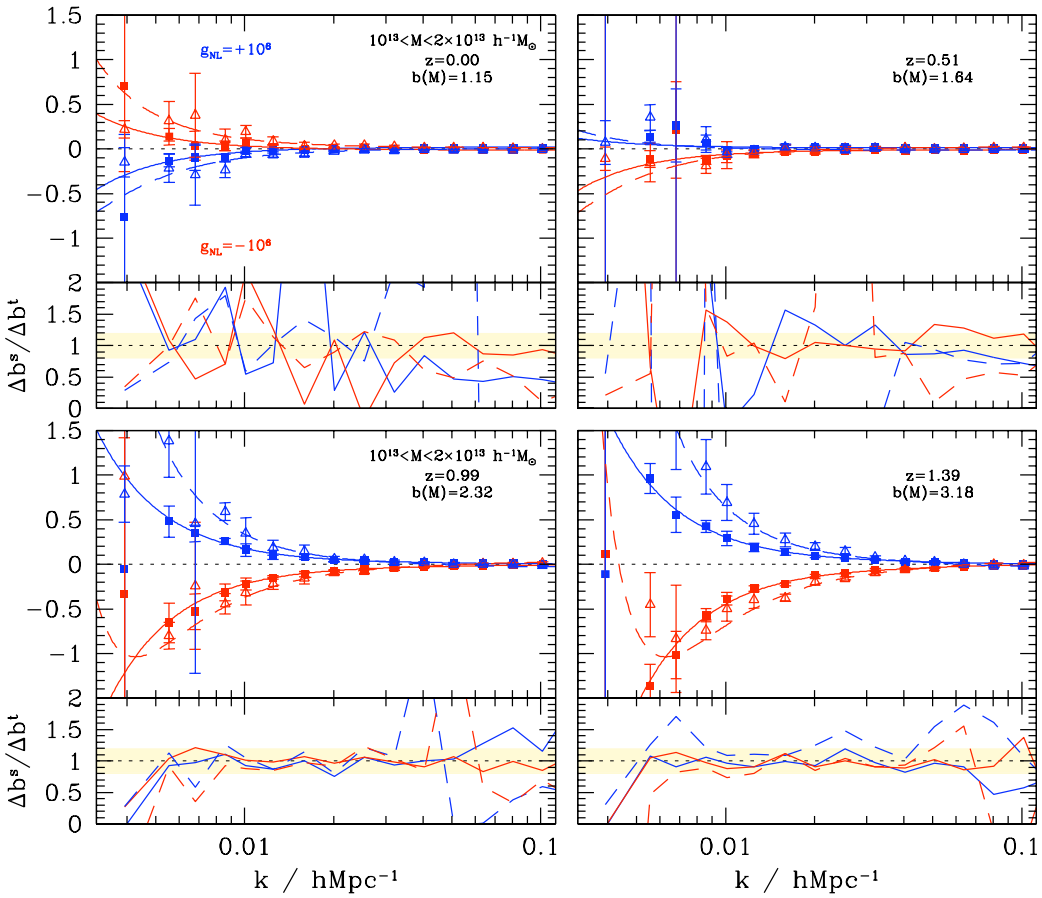

FIG. 8: Same as Fig. 7 but for haloes in the mass range $10^{13} < M < 2 \times 10^{13}$ M$_\odot/h$.

predicted scale-dependent correction Δb_κ is much steeper than measured from the halo samples. In order to improve the agreement with the numerical data, we modify the above relation as follows :

$$\Delta b(k, g_{\rm NL}) = \epsilon_\kappa \, \Delta b_\kappa(k, g_{\rm NL}) + \left[\Delta b_{\rm I}(g_{\rm NL}) + \epsilon_{\rm I}\right] , \quad (27)$$

and treat ϵ_κ and $\epsilon_{\rm I}$ as free parameters that we fit to our measurements of the cross-power spectrum (weighted by the scatter among 5 realisations) in the range $0.005 \leq k \leq 0.03$ hMpc^{-1} where the scale-dependent effect is largest. The bottom panel of Fig. 5 shows the resulting best-fit contributions $\epsilon_\kappa \Delta b_\kappa$ and $\Delta b_{\rm I} + \epsilon_{\rm I}$ for the halo sample mentioned above. As seen in Fig. 6, ϵ_κ and $\epsilon_{\rm I}$ appear to depend mainly upon the linear halo bias $b(M)$ and the coupling parameter $g_{\rm NL}$, although dependencies on redshift or other halo observables are not excluded (The data is too noisy for a reliable estimate of these). The most striking feature of Fig. 6 is the functional dependence of ϵ_κ on $b(M)$ and $g_{\rm NL}$. Firstly, ϵ_κ is a monotonically increasing function of the bias and never reaches unity, even for the most biased samples for which the high peak approximation should be valid. Secondly, ϵ_κ is noticeably larger for $g_{\rm NL} = -10^6$, suggesting thereby that second (and higher) order contributions to the scale-dependent bias may be important. Furthermore, for $b \lesssim 1.5$ where the high peak approximation breaks down, there is some evidence that the effect reverses sign. The bottom panel of Fig. 6 shows that the scale-independent correction has sign opposite to that of $g_{\rm NL}$, in agreement with theoretical expectations from the peak-background split (see Sec.III A). However, whereas for $b \lesssim 3$ the magnitude of the correction is comparable to that predicted by Eq. (24), it is considerably larger for $b \gtrsim 3$, reaching up to 5-10 per cent of the linear halo bias.

Assuming ϵ_κ is a function of $b(M)$ and $g_{\rm NL}$ only and asymptotes to a constant in the highly biased limit, we find that the following parametrised form

$$\epsilon_\kappa(b, g_{\rm NL}) = c_1 - c_2 \, g_{\rm NL} - \frac{c_3}{1 + \exp(c_4 b)} \quad (28)$$

captures reasonably well the increase of ϵ_κ with halo bias for $1.5 < b(M) < 7$. The best-fit values of the parameters

are

$$c_1 = 0.59 \pm 0.03, \quad c_2 = (6.0 \pm 0.9) \times 10^{-8} \qquad (29)$$
$$c_3 = 2.1 \pm 0.5, \quad c_4 = 0.88 \pm 0.13 \, .$$

We do not provide a fitting formula for $\epsilon_{\rm I}$ (or $\Delta b_{\rm I} + \epsilon_{\rm I}$) since it is not directly measurable in real data.

Since both the kurtosis of the initial density field and the mass function of dark matter haloes are in fairly good agreement with theoretical expectations, the discrepancy in the scale-dependent bias $\Delta b_\kappa(k, g_{\rm NL})$ indicates that it is the high peak approximation considered here which is inaccurate, even in the limit $b(M) \gg 1$ where it is supposed to work best. Our perturbative approach may be one of the reasons for this mismatch. Namely, we have derived the scale-dependent bias $\Delta b_\kappa(k, g_{\rm NL})$ under the assumption that the non-Gaussian correction to the halo power spectrum is small whereas, for most of the bias range covered by our halo catalogues, the effect is in fact already very large at $k \lesssim 0.01$ hMpc^{-1}. Note, however, that for the quadratic coupling $f_{\rm NL}\phi^2$, this perturbative treatment predicts an effect of the right magnitude [53]. Explaining these findings clearly requires a better theoretical understanding, which we leave for a future investigation. Notwithstanding this, the phenomenological prescription (27) with parameters ϵ_κ and $\epsilon_{\rm I}$ fitted to the data provides, as we will see below, a good description of the large-scale halo power spectrum in simulations of $g_{\rm NL}$ models.

2. *Non-Gaussian bias from auto- and cross-power spectra*

We have measured auto- and cross-power spectra for a range of halo masses and redshifts spanning the range $0 < z < 2$. The ratios defined in Eq.(25) are shown in Figs 7 and 8 as a function of wavenumber for the mass threshold $M > 2 \times 10^{13}$ M$_\odot/h$ and the mass bin $10^{13} < M < 2 \times 10^{13}$ M$_\odot/h$, respectively. The fractional deviation $\Delta b^s/\Delta b^t$ is also shown at the bottom of each panel. The shaded region indicates a departure less than 20 per cent. Error bars denote the scatter around the mean and, therefore, may underestimate the true errors as they are computed from a small number of realisations. Note that, in order to reduce the impact of sampling variance, we first compute the ratios $P_{\rm mh}(k, g_{\rm NL})/P_{\rm mh}(k, 0)$ and $P_{\rm hh}(k, g_{\rm NL})/P_{\rm hh}(k, 0)$ for each realisation before calculating the average.

As we can see, once ϵ_κ and $\epsilon_{\rm I}$ are fitted to the ratio of cross-power spectra, the theoretical prediction Eq. (27) provides a reasonable description of the non-Gaussian bias in the halo power spectrum $P_{\rm hh}$, indicating that non-Gaussianity does not generate much stochasticity and the predicted scaling $\Delta b_\kappa(k, g_{\rm NL}) \propto k^{-2} T(k)^{-1}$ applies equally well for the auto- and cross-power spectrum. This was also found to be true in $f_{\rm NL}$ models [53]. The inclusion of a scale-independent correction $\Delta b_{\rm I} + \epsilon_{\rm I}$ significantly improve the agreement at $k \lesssim 0.03$ hMpc^{-1}. For the highly biased samples $b > 4$ however, this correction is so large that the non-Gaussian bias shift reverses sign at wavenumber $k \gtrsim 0.05$ hMpc^{-1}. Such an effect is not seen in the simulations, but we expect large deviations from the relation (27) in that range of wavenumber, where second- and higher-order corrections induced by the cubic coupling $g_{\rm NL}\phi^3$ together with the nonlinear bias created by the gravitational evolution of matter density fluctuations may become important. Even though the data is noisier due to the low number density of haloes, it is worth noting that, for the highly biased samples at $k \lesssim 0.01$ hMpc^{-1}, the cross-power spectrum $P_{\rm mh}(k, g_{\rm NL} = -10^6)$ goes negative while $P_{\rm hh}(k, g_{\rm NL} = -10^6)$ remains positive and increases sharply, in agreement with the analytic prediction. Still, there is some evidence that the ratio $P_{\rm hh}(k, g_{\rm NL} = -10^6)/P_{\rm hh}(k, 0) - 1$ saturates at a value noticeably larger than -1 before the sharp upturn, whereas our model predicts $2\delta\sigma_8/\sigma_8 - 1 \approx -0.96$ at the minimum.

Fig. 8 further explore the effect in the low mass samples, for which the $z = 0$ haloes with $b(M) \approx 1.15$ constitute an almost unbiased sample of the density field. In this case, the sign of the scale-dependent contribution is reversed, namely, the large-scale halo power spectrum in simulations of $g_{\rm NL} = -10^6$ is enhanced relative to that of the Gaussian ones. This is in rough agreement with the theory, which predicts a similar effect for $b(M) < 1$. Again, haloes with a similar bias also have a comparable scale-dependent and scale-independent bias regardless of mass or redshift. Finally, note that the sample at $z = 1.39$ shown in Fig. 8 corresponds closely to the quasar sample used by [48], for which $z = 1.8$ and $b = 2.7$.

IV. CONSTRAINTS ON THE COUPLING PARAMETER $g_{\rm NL}$

A. Constraints on $g_{\rm NL}$ from current large-scale structure data

Reference [48] took advantage of the scale-dependence of the bias to constrain $f_{\rm NL}$ from a sample of highly biased luminous red galaxies (LRGs) and quasars (QSOs). It is straightforward to translate their 2-σ limit $-29 < f_{\rm NL} < +69$ into a constraint on $g_{\rm NL}$ since the non-Gaussian scale-dependent bias $\Delta b_\kappa(k, g_{\rm NL})$ has the same functional form as $\Delta b_\kappa(k, f_{\rm NL})$.

Constraints will arise mostly from the QSO sample at median redshift $z = 1.8$, which covers a large comoving volume and is highly biased, $b = 2.7$. In light of our results (see Fig. 6), we expect the parameter $\epsilon_\kappa(b, g_{\rm NL})$ to vary with $g_{\rm NL}$. However, in order to simplify the analysis, we will assume that, at fixed b, $\epsilon_\kappa(b, g_{\rm NL})$ is given by the mean of $\epsilon_\kappa(b, g_{\rm NL} = \pm 10^6)$. For a sample with bias $b \sim 2.7$, this implies $\epsilon_\kappa \simeq 0.4$. Furthermore, assuming the typical mass of QSO-hosting haloes is $\sim 10^{13}$ M$_\odot/h$ yields $S_3^{(1)}(M) \simeq 2.3 \times 10^{-4}$. Hence, the multiplicative factor $(1/4)\, \delta_{\rm c}(z) \epsilon_\kappa S_3^{(1)}(M)$ is approx-

imately $\simeq 8.4 \times 10^{-5}$. Our limits on $g_{\rm NL}$ thus are

$$-3.5 \times 10^5 < g_{\rm NL} < +8.2 \times 10^5 \qquad (30)$$

at 95% confidence level. The scale-independent correction $\Delta b_{\rm I} + \epsilon_{\rm I}$ is not directly measured as it adds up to the bias b which is fitted to the data. For the limits obtained here, $|\Delta b_{\rm I} + \epsilon_{\rm I}|$ should be much smaller than b and can thus be ignored. Note also that, whereas the non-Gaussian bias scales as $D(z)^{-1}$ in $f_{\rm NL}$ models, we have $\Delta b(k, g_{\rm NL}) \propto D(z)^{-2}$ for $g_{\rm NL}$ non-Gaussianity, so one can achieve relatively larger gains from measurements of high redshift tracers. In fact, the extent to which one can improve the observational bounds will strongly depend on our ability to minimize the impact of sampling variance caused by the random nature of the wavemodes, and the shot-noise caused by the discrete nature of the tracers. By comparing differently biased tracers of the same surveyed volume [51] and suitably weighting galaxies (e.g. by the mass of their host halo) [80, 81], it should be possible to circumvent these problems and considerably improve the detection level.

B. Predictions for future LSS surveys

References [50, 51, 64, 82] applied the Fisher matrix formalism to forecast constraints on $f_{\rm NL}$ from forthcoming galaxy redshift surveys. Here, we will simply try to estimate the detection limit for $g_{\rm NL}$. Following [50, 64], we consider a (nearly spherical) survey of volume V. Assuming the Fourier modes are still uncorrelated and Gaussian distributed, the total signal-to-noise squared reads

$$\left(\frac{S}{N}\right)^2 \approx \frac{V}{4\pi^2} \int_{k_{\rm min}}^{k_{\rm max}} dk\, k^2 \left[\left(1 + \frac{\Delta b_\kappa}{b}\right)^2 - 1\right]^2 \qquad (31)$$

in the limit where sampling variance dominates the errors. Here, $k_{\rm min} \sim \pi/V^{1/3}$ is the smallest wavemode accessible and $k_{\rm max}$ is not necessarily finite since the integral does converge as one takes $k_{\rm max}$ to infinity. Substituting the expression Eq. (23) for the scale-dependent bias $\Delta b_\kappa(k, g_{\rm NL})$ and setting $T(k) \equiv 1$ over the wavenumber range across which the integral is performed, we arrive at

$$\left(\frac{S}{N}\right)^2 \approx \frac{V}{\pi^2} (k_\star^2)^2 \left(\frac{1}{k_{\rm min}} - \frac{1}{k_{\rm max}}\right) , \qquad (32)$$

where

$$k_\star^2 \simeq 5.0 \times 10^{-12} g_{\rm NL} \epsilon_\kappa \frac{(1 - 1/b)}{D^2(z)} \left(\frac{S_3^{(1)}}{10^{-4}}\right) \; h^2 {\rm Mpc}^{-2} . \qquad (33)$$

We have also assumed $|g_{\rm NL}| \lesssim 10^5$, such that $|k_\star^2|$ is at most of the order of $k_{\rm min}^2$ and the term linear in $\Delta b_\kappa / b$ dominates the signal. When $k_{\rm min} \ll k_{\rm max}$, we can further simplify $(S/N)^2$ to

$$\left(\frac{S}{N}\right)^2 \approx 8.1 \times 10^{-13} g_{\rm NL}^2 \epsilon_\kappa^2 \left(1 - \frac{1}{b}\right)^2 D(z)^{-4} \times \left(\frac{S_3^{(1)}}{10^{-4}}\right)^2 \left(\frac{V}{h^{-3}{\rm Gpc}^3}\right)^{4/3} . \qquad (34)$$

Note the strong sensitivity of the signal-to-noise squared to the growth factor $D(z)$ (For $f_{\rm NL}$ non-Gaussianity, this dependence is only $D(z)^{-2}$).

To highlight the improvement one could achieve with future galaxy surveys, it is useful to first calculate the detection limit for the SDSS LRG sample centred at $z \sim 0.3$ and covering a volume $v \approx 2\ h^{-3}{\rm Gpc}^3$. Assuming a linear bias $b = 2$ and a skewness parameter $S_3^{(1)} \sim 2 \times 10^{-4}$ appropriate for haloes of mass $M \sim 10^{12} - 10^{13}\ {\rm M}_\odot/h$, the minimum $g_{\rm NL}$ detectable at the 1-σ level is $\simeq 10^6$ for a correction factor $\epsilon_\kappa = 0.3$ which we read off from Fig. 6. For a survey configuration analogous to SDSS-III/BOSS [2], with central redshift $z = 0.5$ and a comoving volume $V = 6\ h^{-3}{\rm Gpc}^3$, the minimum $g_{\rm NL}$ would be $\sim 4 \times 10^5$ for galaxies tracing haloes of similar mass and bias. Finally, for a configuration like EUCLID [3] with a $V = 100\ h^{-3}{\rm Gpc}^3$ survey centred at $z = 1.4$, the detection limit would be $\sim 2.1 \times 10^4$. Clearly, these limits are only indicative: they may be significantly improved by selecting highly biased, high redshift (single- or multi-)tracers. Nevertheless, this shows that future galaxy surveys should furnish interesting constraints on the size of the cubic coupling $g_{\rm NL}\phi^3$.

C. Predictions for CMB temperature anisotropies

The CMB trispectrum provides an alternative probe of local, non-quadratic correction to the Gaussian curvature perturbations, so it is interesting to assess the sensitivity of this statistics to the nonlinear parameter $g_{\rm NL}$.

The temperature anisotropy field is conveniently decomposed into spherical harmonics, $\Delta T(\hat{\mathbf{n}})/T = \sum_{lm} a_l^m Y_l^m(\hat{\mathbf{n}})$. As shown in [29, 30], statistical isotropy and invariance under parity transformation $\hat{\mathbf{n}} \to -\hat{\mathbf{n}}$ implies that the 4-point correlation of the spherical harmonic coefficients a_l^m takes the form

$$\langle a_{l_1}^{m_1} a_{l_2}^{m_2} a_{l_3}^{m_3} a_{l_4}^{m_4} \rangle = \sum_{LM} (-1)^M \begin{pmatrix} l_1 & l_2 & L \\ m_1 & m_2 & -M \end{pmatrix} \times \begin{pmatrix} l_3 & l_4 & L \\ m_3 & m_4 & M \end{pmatrix} Q_{l_3 l_4}^{l_1 l_2}(L) . \qquad (35)$$

[2] www.sdss3.org
[3] http://sci.esa.int/science-e/www/object/index.cfm?fobjectid=42266

Here, $Q^{l_1 l_2}_{l_3 l_4}(L)$ is the angular average trispectrum and brackets are Wigner-3j symbols. Statistical homogeneity also implies that $Q^{l_1 l_2}_{l_3 l_4}(L)$ is independent of position. The connected part of the trispectrum, $T^{l_1 l_2}_{l_3 l_4}(L)$, encodes information about non-Gaussianity and is obtained by subtracting a Gaussian piece constructed from the power spectra C_l. Eq.(35) can be inverted with the aid of the orthogonality of the Wigner-3j symbols to form an estimator for the CMB trispectrum.

The signal-to-noise for the CMB trispectrum $T^{l_1 l_2}_{l_3 l_4}(L)$ summed up to a certain $l_{\rm max}$ is [30]

$$\left(\frac{S}{N}\right)^2 (< l_{\rm max}) \approx \sum_{l_1 > l_2 > l_3 > l_4}^{l_{\rm max}} \sum_L \frac{|T^{l_1 l_2}_{l_3 l_4}(L)|^2}{(2L+1) C_{l_1} C_{l_2} C_{l_3} C_{l_4}} \tag{36}$$

when cosmic variance dominates the errors. Otherwise, one shall include a contribution from the power spectrum of the detector noise to the C_l. Galactic foreground subtraction on a fraction $1 - f_{\rm sky}$ would further reduce $(S/N)^2$ by a factor of $f_{\rm sky}$.

Neglecting the ISW effect, the Sachs-Wolfe provides a useful order-of-magnitude estimate of the signal-to-noise as long as $l_{\rm max}$ does not exceed $\lesssim 100$ [7, 30, 31, 83]. The calculation is performed in Appendix B. We find that the signal-to-noise can be recast into the compact form

$$\left(\frac{S}{N}\right)^2 (< l_{\rm max}) = \frac{9}{2} g^2_{\rm NL} A^2_\phi \left\{ \frac{1}{6} \int_{-1}^{+1} dx\, s^3_{l_{\rm max}}(x) t_{l_{\rm max}}(x) + \frac{1}{2} \int_{-1}^{+1} dx\, r^2_{l_{\rm max}}(x) s^2_{l_{\rm max}}(x) \right\} \tag{37}$$

where the auxiliary functions $r_l(x)$, $s_l(x)$ and $t_l(x)$ are defined as

$$r_l(x) = \sum_{k=2}^{l} (2k+1) P_k(x) \tag{38}$$

$$s_l(x) = \sum_{k=2}^{l} \frac{(2k+1)}{k(k+1)} P_k(x) \tag{39}$$

$$t_l(x) = \sum_{k=2}^{l} (2k+1) k(k+1) P_k(x)\ . \tag{40}$$

Here, $P_l(x)$ are Legendre polynomials. Note that we have excluded the monopole and dipole from the summation since these modes are unobservable. We have also assumed a nearly scale-invariant spectrum $n_s \approx 1$.

Figure. 9 shows the signal-to-noise ratio squared in the Sachs-Wolfe approximation for the CMB trispectrum assuming $g_{\rm NL} = 1$. Although this approximation breaks down for $l_{\rm max} \gtrsim 100$, we have extended the calculation up to $l_{\rm max} = 200$ so as to extrapolate more robustly the $l_{\rm max}$-dependence to small angular resolution. A power-law fit to $(S/N)^2$ in the range $50 \leq l_{\rm max} \leq 200$ gives

$$\left(\frac{S}{N}\right)^2 (< l_{\rm max}) \simeq 2.43 \times 10^{-17} g^2_{\rm NL} \left(\frac{A_\phi}{10^{-9}}\right)^2 l^{2.6}_{\rm max}\ . \tag{41}$$

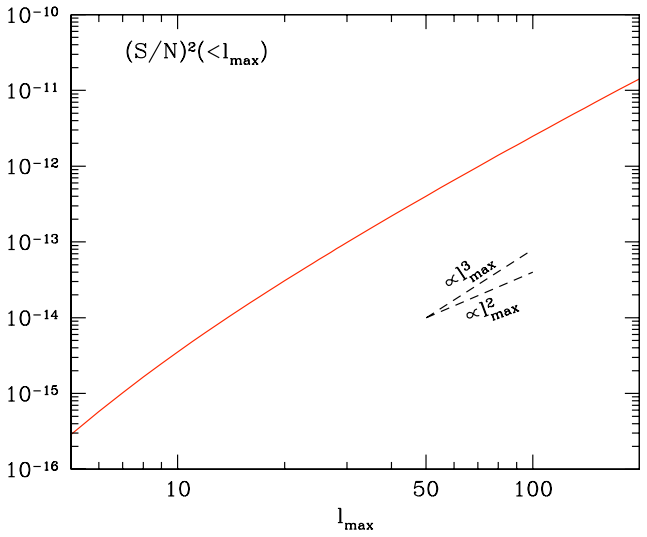

FIG. 9: Signal-to-noise ratio squared for the CMB trispectrum as a function of the maximum multipole $l_{\rm max}$. We have assumed $g_{\rm NL} = 1$ and $f_{\rm sky} = 1$.

Our results appear consistent with the findings of [30] shown in their Fig.2. However, our constant of proportionality is about 20-30 times larger, presumably because they adopted a lower fluctuation amplitude (compare also their prediction for the $f_{\rm NL}$ model with that of [31]). Adding the information encoded in temperature-polarization trispectra may enhance $(S/N)^2$ by a factor of a few [29].

Assuming the scaling Eq.(41) persists well beyond the range over which the Sachs-Wolfe effect dominates, the minimum $g_{\rm NL}$ detectable at 1-σ level is $g_{\rm NL} \simeq 20$, 7.9, 3.2, 1.9 and 1.3×10^4 for $l_{\rm max} = 250$, 500, 1000, 1500 and 2000. A more realistic calculation should include the full radiation transfer function, detector noise etc. In this respect, detailed calculations have shown that, for the quadratic coupling $f_{\rm NL}\phi^2$, $(S/N)^2$ of the CMB bispectrum and trispectrum closely follows the behaviour obtained in the Sachs-Wolfe approximation [30, 31]. It seems reasonable, then, to expect that this is also true for $g_{\rm NL}\phi^3$.

While our predictions are qualitative they show that, for the WMAP CMB temperature measurement [4] (which we approximate as a noise-free experiment with $l_{\rm max} \sim 250$), no detection of a significant trispectrum implies $|g_{\rm NL}| \leq 2 \times 10^5$ at the 1-σ level. This is of the same order as the limit we derived from the QSO sample analyzed by [48]. For a PLANCK-like experiment [5] ($l_{\rm max} \sim 1500$), no evidence for a trispectrum would imply $|g_{\rm NL}| \leq 1.3 \times 10^4$ at the 1-σ level. This is comparable to the detection

[4] http://map.gsfc.nasa.gov/
[5] http://sci.esa.int/science-e/www/area/index.cfm?fareaid=17

limit that could be achieved with an all-sky survey such as EUCLID.

V. EFFECT OF NON-GAUSSIANITY WITH NON-ZERO $f_{\rm NL}$ AND $g_{\rm NL}$

In this Section, we examine the halo multiplicity function and large-scale bias in numerical simulations of structure formation with non-zero coupling parameters $(f_{\rm NL}, g_{\rm NL}) = (\pm 100, -3\times 10^5)$. We show that the results are consistent with those obtained from the simulations with non-vanishing $g_{\rm NL}$ solely.

A. Mass function

It is straightforward to calculate the fractional deviation from the Gaussian mass function, Eq.(18), to non-zero $f_{\rm NL}$ and $g_{\rm NL}$. Again, we start with the MVJ formula and neglect second order corrections such as $(\sigma S_3)^2$ etc. Adjusting the coefficient of the terms $\nu\sigma S_3$ and $\nu^2\sigma^2 S_4$ to that of the small ν expansion obtained by [73], we arrive at

$$R(\nu,{\rm NL}) = \exp\left[\frac{\nu^3}{3!}\sigma S_3 + \frac{\nu^4}{4!}\sigma^2 S_4 + \nu^2\delta\sigma_8\right] \times\left\{1 - \frac{\nu}{2}\sigma S_3 - \frac{\nu}{6}\frac{d(\sigma S_3)}{d\ln\nu} - \frac{\nu^2}{4}\sigma^2 S_4 - \frac{\nu^2}{4!}\frac{d(\sigma^2 S_4)}{d\ln\nu}\right\}, \quad (42)$$

where the shorthand notation NL designates the combination $(f_{\rm NL}, g_{\rm NL})$. In Fig. 10, this theoretical prediction is compared $R(\nu,{\rm NL})$ measured in non-Gaussian simulations of $(f_{\rm NL}, g_{\rm NL}) = (\pm 100, -3\times 10^5)$. We account for the fact that the amplitude of density fluctuations is renormalised by $\delta\sigma_8 \approx 0.0045$. Fig. 10 demonstrates that our approximation is in good agreement with the data, although it slightly overestimates the effect at $z = 2$ when $f_{\rm NL} = -100$. For $f_{\rm NL} = 100$, the positive and negative contributions from the quadratic and cubic coupling, respectively, almost cancel each other and flatten the fractional deviation over most of the mass range probed by the simulations.

The scale-independent bias shift which arises from the change in the mean number density of haloes can again be estimated using the peak-background split. We find

$$\Delta b_{\rm I}({\rm NL}) \approx -\frac{1}{\sigma}\left[\frac{1}{3!}\left(\nu^3 - 3\nu\right)\sigma^2 S_4 + \frac{1}{2}\left(\nu^2 - 1\right)\sigma S_3 + \frac{1}{4!}\left(\nu^3 - 8\nu\right)\frac{d(\sigma^2 S_4)}{d\ln\nu} - \frac{\nu}{4!}\frac{d^2(\sigma^2 S_4)}{d\ln\nu^2} + \frac{1}{6}\left(\nu^2 - 4\right)\frac{d(\sigma S_3)}{d\ln\nu} - \frac{1}{6}\frac{d^2(\sigma S_3)}{d\ln\nu^2} + 2\nu\delta\sigma_8\right] \quad (43)$$

at the first order in the nonlinear parameters $f_{\rm NL}$ and $g_{\rm NL}$.

B. Bias

Having checked that the amount of non-Gaussianity in the mass function is also consistent with our simple theoretical expectation when both $f_{\rm NL}$ and $g_{\rm NL}$ are non-zero, we now turn to the clustering of dark matter haloes. As shown in Appendix A, the non-Gaussian correction to the halo power spectrum can be written down as

$$\Delta P_{\rm hh}(k) = 4 f_{\rm NL} b_{\rm L}^2 \delta_{\rm c}(z)\alpha_M(k) P_\phi(k) + 4 f_{\rm NL}^2 b_{\rm L}^2 \delta_{\rm c}^2(z) P_\phi(k) + \left(g_{\rm NL} + \frac{4}{3} f_{\rm NL}^2\right) \times b_{\rm L}^2 \delta_{\rm c}^2(z) S_3^{(1)}(M)\alpha_M(k) P_\phi(k)\,. \quad (44)$$

If we set $g_{\rm NL} = 0$ and keep only the first two terms in the right-hand side, then the non-Gaussian (Eulerian) halo power spectrum can be cast into the form

$$P_{\rm hh}(k) = \left[b(M) + f_{\rm NL} b_\phi(k)\right]^2 P_\delta(k) \quad (45)$$

where the scale-dependent bias parameter $b_\phi(k)$ is

$$b_\phi(k) = 2\left[b(M) - 1\right]\delta_{\rm c}(z)\,\alpha_M^{-1}(k)\,. \quad (46)$$

Note that reference [64] obtained this relation by considering the halo power spectrum implied by a bias relation that is a local mapping of the density field. In practice, the term proportional to $P_\phi(k)$ is negligible as it contributes only at very small wavenumber $k \lesssim 0.001\ h^{-1}$Mpc. The third term in the right-hand side of Eq.(44) is derived in this paper for the first time. In the case $g_{\rm NL} = 0$, its magnitude relative to the term linear in $f_{\rm NL}$ is $(1/3) f_{\rm NL}\delta_{\rm c}(z) S_3^{(1)}(M)$, which is approximately ~ 0.03 at redshift $z = 1.8$ and for a mass scale $M = 10^{13}\ {\rm M}_\odot/h$. Although its contribution becomes increasingly important at higher redshift, it is fairly small for the values of $f_{\rm NL}$ considered here. Consequently, we shall employ the approximation

$$\Delta b({\rm NL}) = \epsilon_\kappa\,\Delta b_\kappa(k, g_{\rm NL}) + \Delta b_\kappa(k, f_{\rm NL}) + \left[\Delta b_{\rm I}({\rm NL}) + \epsilon_{\rm I}\right]\,. \quad (47)$$

to describe the non-Gaussian bias of dark matter haloes.

The quadratic coupling $f_{\rm NL}\phi^2$ also affect the matter power spectrum at leading order [38, 84], positive values of $f_{\rm NL}$ increasing the small scale power. However, the relative size of this k-dependent correction, $\beta_{\rm m}(k, f_{\rm NL})$, is at a per cent level only in the weakly nonlinear regime $k \lesssim 0.1\ h{\rm Mpc}^{-1}$ [53, 85] and fades rapidly as one goes to larger scales. We will thus neglect it in what follows.

In Fig. 11, the result of measuring ratios of auto- and cross-power spectra in the simulations with $(f_{\rm NL}, g_{\rm NL}) = (\pm 100, -3\times 10^5)$ is shown at $0 < z < 1.5$ for the haloes with $M > 2\times 10^{13}\ {\rm M}_\odot/h$. We do not quote error bars

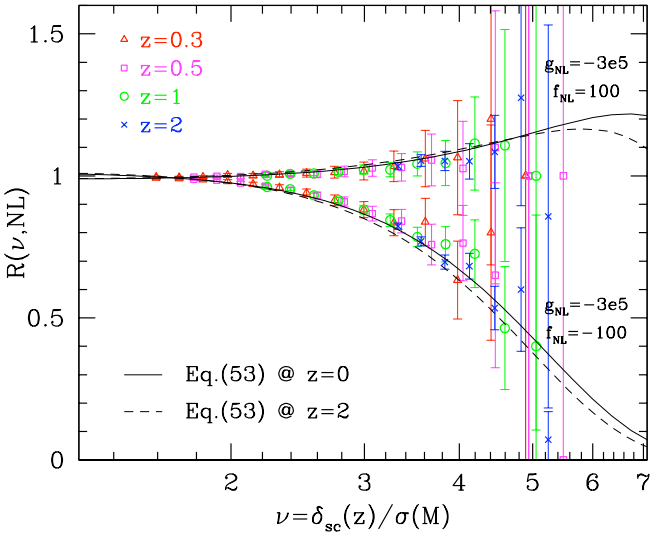

FIG. 10: Fractional correction to the Gaussian multiplicity function of dark matter haloes as a function of the peak height $\nu(M,z)$ for $f_{\rm NL}=\pm100$ and a cubic coupling parameter $g_{\rm NL}=-3\times10^5$. The solid and dashed curves show the theoretical prediction Eq.(42) at $z=0$ and 2, respectively. Error bars denote Poisson errors.

since the data points are obtained by averaging over two realisations only. The solid and dashed curves show the theoretical prediction Eq. (47). The value of the multiplicative factor $\epsilon_\kappa(b,g_{\rm NL})$ was obtained from the four-parameter formula Eq.(28), while $\Delta b_{\rm I}+\epsilon_{\rm I}$ was individually fitted for each halo sample over the wavenumber range $0.005<k<0.03\ h{\rm Mpc}^{-1}$. As can be seen, the theoretical expectation Eq. (47) agrees reasonably well with the numerical data. This demonstrates that the range of validity of the non-Gaussian bias formula Eq. (27) extends to smaller values of $g_{\rm NL}$ as well as models with non-vanishing $f_{\rm NL}$ and $g_{\rm NL}$.

The lowest order, k-dependent corrections to the Gaussian bias induced by the quadratic and the cubic coupling are fully degenerated in the halo power spectrum as they both scale as $\alpha_M^{-1}(k)\propto k^{-2}T(k)^{-1}$. For the values of $f_{\rm NL}$ and $g_{\rm NL}$ and the halo mass range considered here, the ratio $\Delta b_\kappa(k,g_{\rm NL})/\Delta b_\kappa(k,f_{\rm NL})$ increases approximately from 0.25 to 0.5 when the redshift increases from $z=0$ to 2. It is unclear whether higher order corrections could help breaking such a degeneracy. A more promising alternative may be to measure the bispectrum of dark matter haloes, which carries much more information about the shape of the primordial three-point function than the power spectrum of bias tracers [40, 41]. However, this is beyond the scope of this paper.

VI. DISCUSSION

In this paper we explored the effect of a local cubic coupling $g_{\rm NL}\phi^3$ on the mass function and bias of dark matter haloes. We derived analytical expressions for these statistics and tested them against the outcome of numerical simulations.

We showed that current theoretical predictions of the non-Gaussian correction to the mass function reasonably agree with the simulations. The LV formula [73] appears to provide a better fit to the data than the MVJ formula [74], in agreement with some of the literature on the subject [46, 86]. The two approximations can be combined to provide an accurate description if one adjusts the low-ν expansion of the latter so as to match that of the former.

We found that the magnitude of the non-Gaussian scale-dependent bias $\Delta b_\kappa(k,g_{\rm NL})$ is suppressed relative to a theoretical prediction based on the statistics of highly overdense regions, even on linear scales $k\lesssim0.01\ h{\rm Mpc}^{-1}$. This suppression is stronger for the low biased samples $b\lesssim3$ and, at fixed value of b, for positive values of $g_{\rm NL}$. We were able to fit the measured halo bias at the expense of introducing two free parameters, ϵ_κ and $\epsilon_{\rm I}$, that depend mostly on the halo bias $b(M)$ and the coupling parameter $g_{\rm NL}$. These parameters quantify the departure from the theoretical scale-dependent and scale-independent non-Gaussian bias correction, respectively. We provide a simple fitting formula for $\epsilon_\kappa(b,g_{\rm NL})$, Eq.(28), which should be used when analyzing observational data. In non-Gaussian simulations of the $f_{\rm NL}$ type, the data also hint at a (possibly $f_{\rm NL}$-dependent) suppression of the non-Gaussian scale-dependent bias relative to theory for wavemodes $k\lesssim0.03\ h{\rm Mpc}^{-1}$ [53, 54, 55], but the effect is much weaker than seen in our simulations of $g_{\rm NL}$ models. Clearly, these results require a better theoretical modelling of the non-Gaussian halo bias.

Reference [55] argued that both the MVJ and LV analytic formula can be reconciled with measurements of the non-Gaussian fractional correction to the mass function once non-spherical collapse is included. In practice, the critical density for collapse is replaced by $\delta_{\rm c}\to\sqrt{q}\delta_{\rm c}$, where the value $q=0.75$ is obtained from a fit to the mass function measured in simulations [87]. Reference [88] claimed that such a relation is a consequence of the diffusive nature of the critical threshold for collapse. Their model predicts $q\simeq0.8$, in good agreement with the findings of [55]. However, we found that substituting $\delta_{\rm c}\to\sqrt{q}\delta_{\rm c}$ in Eq.(18) only modestly improve the agreement with the data. Regarding the non-Gaussian bias, it is not obvious how one could justify the replacement $\delta_{\rm c}\to\sqrt{q}\delta_{\rm c}$ given that the linear bias of our (Gaussian) halo samples converges towards the spherical collapse prediction $\nu^2/\delta_{\rm c}$ for large peak height.

A important ingredient is the choice of the halo identification algorithm. While we used a spherical overdensity (SO) finder, reference [88] considered a Friends-of-Friends (FoF) finder with a linking length $b=0.2$. The question of how the spherical overdensity masses can be

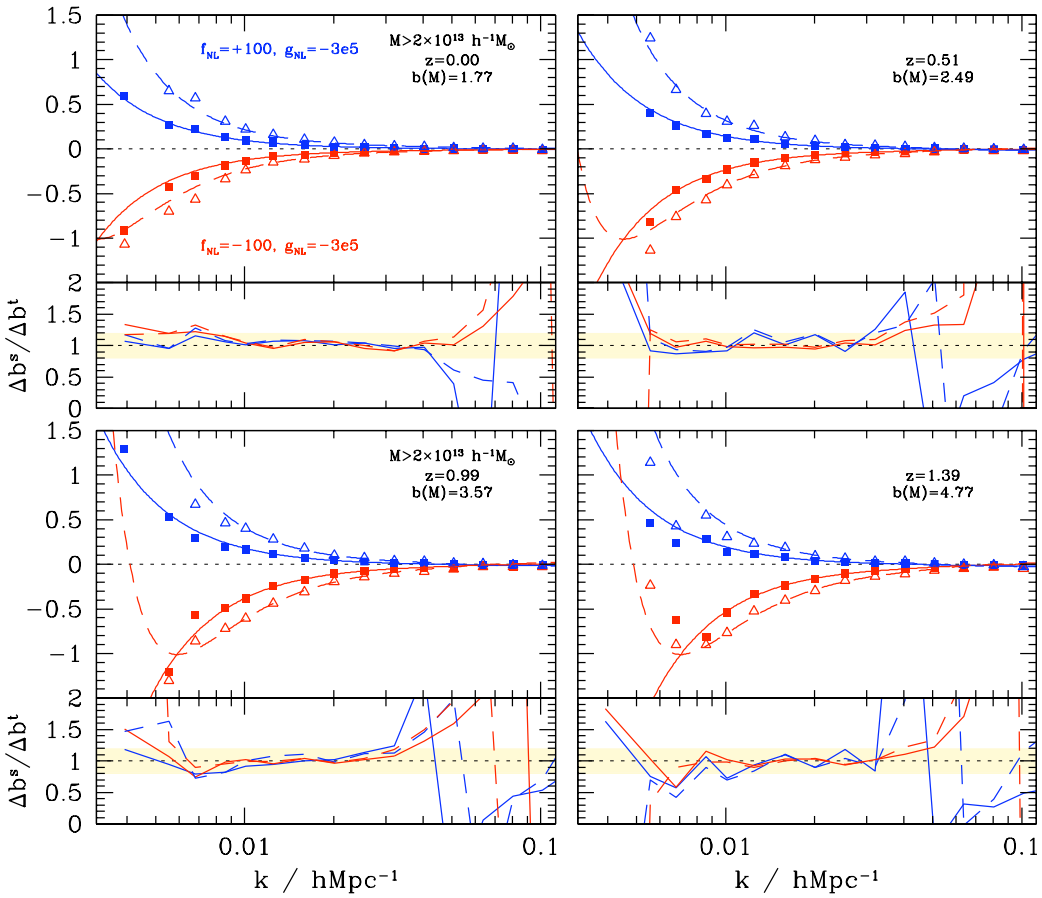

FIG. 11: Non-Gaussian bias correction measured in the simulations with $(f_{\rm NL}, g_{\rm NL}) = (\pm 100, -3 \times 10^5)$ for haloes of mass $M > 2 \times 10^{13}$ $M_\odot/h$. Error bars are not shown as the data points are averaged over two realisations solely.

mapped onto friends-of-friends masses remains a matter of debate [89]. Clealy however, since the peak height depends on the halo mass M through the variance $\sigma(M)$, any systematic difference will be reflected in the value of ν associated to a specific halo sample. This will in turn affects the size of the fractional deviation from the Gaussian mass function at some specified peak height. The sensitivity of the non-Gaussian mass function and bias to the halo finder will be presented elsewhere.

The observational bound on $f_{\rm NL}$ inferred by [48] from the clustering of a high redshift sample of quasars can be straightforwardly translated into a limit on $g_{\rm NL}$ since $\Delta b_\kappa(k, g_{\rm NL})$ also scales as $k^{-2}T(k)^{-1}$ at low wavenumber. We have obtained

$$-3.5 \times 10^5 < g_{\rm NL} < +8.2 \times 10^5 \quad (95\%). \qquad (48)$$

These are the first limits derived on $g_{\rm NL}$. While they are too weak to provide interesting constraints on inflationary scenarios such as the curvaton model, future all-sky redshift surveys should improve them by a factor of ~ 100. Future CMB observations, including PLANCK, should also improve the limits derived here by an order of magnitude. With these improvements we expect that, in the next decade, realistic models of cubic type non-Gaussianity will be tested with real observations.

Acknowledgements

We thank Paolo Creminelli and Leonardo Senatore for useful discussions. We acknowledge support from the Swiss National Foundation under contract No. 200021-116696/1 and WCU grant R32-2008-000-10130-0.

APPENDIX A: NON-GAUSSIAN BIAS IN THE HIGH PEAK LIMIT

In this Appendix, we detail the derivation of the scale-dependent bias correction induced by the $g_{\rm NL}$ coupling to the two-point correlation of dark matter haloes. We follow [47] and approximate the latter by the two-point

correlation $\xi_{\rm hh}(\mathbf{r})$ of regions of the smoothed density field δ_M with a peak height $\nu \gg 1$.

1. case $g_{\rm NL} \neq 0$ only

In this case, only the four-point correlations of the density field contribute at the first order. The leading-order correction to the correlation of tresholded regions thus reads as

$$\Delta\xi_{\rm hh} = \frac{\nu^4}{\sigma^4}\left[\frac{1}{3}\xi^{(4)}(\mathbf{x}_1,\mathbf{x}_1,\mathbf{x}_1,\mathbf{x}_2) + \frac{1}{4}\xi^{(4)}(\mathbf{x}_1,\mathbf{x}_1,\mathbf{x}_2,\mathbf{x}_2)\right] . \tag{A1}$$

The four-point correlations $\xi^{(4)}$ are Fourier transform of the trispectrum of the density field, $T_\delta(\mathbf{k}_1,\mathbf{k}_2,\mathbf{k}_3,\mathbf{k}_4)$, with conservation of momentum enforced. Linearly extrapolating the density field to present epoch, the latter can be expressed as

$$T_\delta(\mathbf{k}_1,\mathbf{k}_2,\mathbf{k}_3,\mathbf{k}_4) = \left(\prod_{i=1}^{4}\alpha_M(k_i)\right) T_\Phi(\mathbf{k}_1,\mathbf{k}_2,\mathbf{k}_3,\mathbf{k}_4) , \tag{A2}$$

where the expression for the trispectrum of primordial curvature perturbation

$$T_\Phi(\mathbf{k}_1,\mathbf{k}_2,\mathbf{k}_3,\mathbf{k}_4) = 6g_{\rm NL}\big[P_\phi(k_1)P_\phi(k_2)P_\phi(k_3)+(\text{cyclic})\big] \tag{A3}$$

follows straightforwardly from the Fourier mode relation

$$\Phi(\mathbf{k}) = \phi(\mathbf{k}) + g_{\rm NL}\int\frac{d^3k_1}{(2\pi)^3}\int\frac{d^3k_2}{(2\pi)^3}\phi(\mathbf{k}_1)\phi(\mathbf{k}_2)\phi(\mathbf{k}-\mathbf{k}_1-\mathbf{k}_2) . \tag{A4}$$

Density and curvature perturbations are related through the Poisson equation, whose scale-dependence is reflected in the function $\alpha_M(k) = \alpha_R(k, z=0)$ defined in Eq. (6). Combining these relations gives

$$\xi^{(4)}(\mathbf{x}_1,\mathbf{x}_1,\mathbf{x}_1,\mathbf{x}_2) = 6g_{\rm NL}\left(\prod_{i=1}^{3}\int\frac{d^3k_i}{(2\pi)^3}\,\alpha_M(k_i)P_\phi(k_i)\right)\left[1+3\,\frac{P_\phi(k_{123})}{P_\phi(k_3)}\right]\alpha_M(k_{123})\,e^{i\mathbf{k}_{123}\cdot\mathbf{r}} \tag{A5}$$

$$\xi^{(4)}(\mathbf{x}_1,\mathbf{x}_1,\mathbf{x}_2,\mathbf{x}_2) = 6g_{\rm NL}\left(\prod_{i=1}^{3}\int\frac{d^3k_i}{(2\pi)^3}\,\alpha_M(k_i)P_\phi(k_i)\right)\left[1+2\frac{P_\phi(k_{123})}{P_\phi(k_1)}+\frac{P_\phi(k_{123})}{P_\phi(k_3)}\right]\alpha_M(k_{123})\,e^{i\mathbf{k}_{12}\cdot\mathbf{r}} , \tag{A6}$$

where we have defined $\mathbf{k}_{ij\cdots l} = \mathbf{k}_i + \mathbf{k}_j + \cdots + \mathbf{k}_l$ for shorthand convenience. Since we will examine the effect of non-Gaussianity on Fourier space statistics only, we take the Fourier transform of the four-point functions. After some simplification, we arrive at

$$\begin{aligned}\int d^3r\,\xi^{(4)}(\mathbf{x}_1,\mathbf{x}_1,\mathbf{x}_1,\mathbf{x}_2)e^{-i\mathbf{k}\cdot\mathbf{r}} &= 6g_{\rm NL}\alpha_M(k)P_\phi(k)\int\frac{d^3k_1}{(2\pi)^3}\alpha_M(k_1)P_\phi(k_1)\int\frac{d^3k_2}{(2\pi)^3}\alpha_M(k_2)P_\phi(k_2)\\ &\quad\times\alpha_M\big(|\mathbf{k}+\mathbf{k}_{12}|\big)\left[3+\frac{P_\phi\big(|\mathbf{k}+\mathbf{k}_{12}|\big)}{P_\phi(k)}\right]\end{aligned} \tag{A7}$$

$$\begin{aligned}\int d^3r\,\xi^{(4)}(\mathbf{x}_1,\mathbf{x}_1,\mathbf{x}_2,\mathbf{x}_2)e^{-i\mathbf{k}\cdot\mathbf{r}} &= 6g_{\rm NL}\int\frac{d^3k_1}{(2\pi)^3}\alpha_M(k_1)\alpha_M(|\mathbf{k}+\mathbf{k}_1|)P_\phi(k_1)P_\phi\big(|\mathbf{k}+\mathbf{k}_1|\big)\int\frac{d^3k_2}{(2\pi)^3}\alpha_M(k_2)\\ &\quad\times\alpha_M\big(|\mathbf{k}+\mathbf{k}_2|\big)P_\phi(k_2)\left[1+2\frac{P_\phi\big(|\mathbf{k}+\mathbf{k}_2|\big)}{P_\phi\big(|\mathbf{k}+\mathbf{k}_1|\big)}+\frac{P_\phi\big(|\mathbf{k}+\mathbf{k}_2|\big)}{P_\phi(k_2)}\right] .\end{aligned} \tag{A8}$$

For realistic values of the spectral index ($n_s \sim 1$), the products $\alpha_M(|\mathbf{k}+\mathbf{k}_i|)P_\phi(|\mathbf{k}+\mathbf{k}_i|)$ appearing in the right-hand side of the above equalities formally diverges whenever $\mathbf{k}+\mathbf{k}_1 = 0$ due to the ultraviolet divergence of

$P_\phi(k)$. To cure this problem, one can set $P_\phi(k) = 0$ for sufficiently small wavenumbers or excise a thin shell centred at wavenumber k_i from the integral. In the large-scale limit $k \ll k_i$, the ratio $P_\phi(|\mathbf{k}+\mathbf{k}_i|)/P_\phi(k)$ vanishes whereas $P_\phi(|\mathbf{k}+\mathbf{k}_i|)/P_\phi(k_i)$ tends towards unity. In this case, the above expressions reduce to

$$\int d^3r\, \xi^{(4)}(\mathbf{x}_1,\mathbf{x}_1,\mathbf{x}_1,\mathbf{x}_2)e^{-i\mathbf{k}\cdot\mathbf{r}} \approx 3g_{\rm NL}\,\sigma^4 S_3^{(1)}(M)\,\alpha_M(k)P_\phi(k) + 6g_{\rm NL}\alpha_M(k)\int\frac{d^3k_1}{(2\pi)^3}\alpha_M(k_1)P_\phi(k_1)\int\frac{d^3k_2}{(2\pi)^3}\alpha_M(k_2)P_\phi(k_2)\alpha_M(k_{12})P_\phi(k_{12})\,, \quad \text{(A9)}$$

and

$$\int d^3r\, \xi^{(4)}(\mathbf{x}_1,\mathbf{x}_1,\mathbf{x}_2,\mathbf{x}_2)e^{-i\mathbf{k}\cdot\mathbf{r}} \approx 24g_{\rm NL}\,\sigma^2\int\frac{d^3k_1}{(2\pi)^3}\,\alpha_M^2(k_1)P_\phi^2(k_1)\,. \quad \text{(A10)}$$

Only the first term in the right-hand side of Eq.(A9) is not well behaved in the limit $k \to 0$ where it becomes proportional to k^{n_s-2}. The second scales as k^2, while the Fourier transform of $\xi^{(4)}(\mathbf{x}_1,\mathbf{x}_1,\mathbf{x}_2,\mathbf{x}_2)$ asymptotes to a constant. A similar decomposition also arises in $f_{\rm NL}$ models. For this type of non-Gaussianity, the first order correction is furnished by the three-point function $\xi^{(3)}(\mathbf{x}_1,\mathbf{x}_1,\mathbf{x}_2)$, whose Fourier transform can be split into the familiar term $2f_{\rm NL}\sigma^2\alpha_M(k)P_\phi(k)$, and a second piece given by

$$\frac{1}{2}f_{\rm NL}\alpha_M(k)\int\frac{d^3k_1}{(2\pi)^3}\,\alpha_M^2(k_1)P_\phi^2(k_1)\,. \quad \text{(A11)}$$

In both quadratic and cubic local non-Gaussianity, the term proportional to $\alpha_M(k)$ can be neglected since, at the pivot point $k = k_0$, its magnitude relative to the term involving $\alpha_M(k)P_\phi(k)$ is only $\mathcal{O}(0.01)$ and $\mathcal{O}(10^{-6})$, respectively. Moreover, it decreases as one goes to larger scales. By contrast, it is not so obvious how to handle the term (A10). In the non-Gaussian halo power spectrum, this term would appear multiplied by $\nu^4/(4\sigma^4)$,

$$6\,g_{\rm NL}b_{\rm L}^2\frac{\delta_{\rm c}^2(z)}{\sigma^2}\int\frac{d^3k_1}{(2\pi)^3}\alpha_M^2(k_1)P_\phi^2(k_1) \simeq 6\times10^{-4}g_{\rm NL}b_{\rm L}^2\,\frac{D^2(0)}{D^2(z)}\left(\frac{M}{10^{13}\ {\rm M}_\odot/h}\right)^{0.375}. \quad \text{(A12)}$$

The approximation (second line) holds for $10^{13} \le M \le 10^{14}\ {\rm M}_\odot/h$. For $g_{\rm NL} = 10^6$ and $b_{\rm L} \gtrsim 3$, this can be much larger than the typical shot-noise correction applied to the halo power spectra we measure in the simulations (see below). For $g_{\rm NL} = -10^6$, this will certainly produce a halo power spectrum which is negative at sufficiently low wavenumber. It is plausible that higher order counter-terms in the expansion Eq.(21) renormalises its value. However, such a calculation is beyond the scope of this paper, so the simplest choice is to ignore this term in the following of the analysis. Hence, we can approximate the non-Gaussian correction $\Delta P_{\rm hh}$ in the limit of long wavelength $k \ll 1$ by the Fourier transform of $\nu^4\xi^{(4)}(\mathbf{x}_1,\mathbf{x}_1,\mathbf{x}_2,\mathbf{x}_2)/3\sigma^4$, Eq. (22).

2. case $g_{\rm NL}$ and $f_{\rm NL}$ non-zero

In addition to the first order trispectrum induced by $g_{\rm NL}\phi^3$, Eq. (A3), the quadratic coupling $f_{\rm NL}\phi^2$ generates the bispectrum at leading order

$$B_\Phi(\mathbf{k}_1,\mathbf{k}_2,\mathbf{k}_3) = 2f_{\rm NL}\big[P(k_1)P(k_2) + ({\rm cyclic})\big]\,, \quad \text{(A13)}$$

and an additional, albeit second order, contribution to the trispectrum [90, 91, 92],

$$T_\Phi(\mathbf{k}_1,\mathbf{k}_2,\mathbf{k}_3,\mathbf{k}_4) = 4f_{\rm NL}^2\big[P_\phi(k_{13})P_\phi(k_3)P_\phi(k_4) + 11\ {\rm permutations}\big]\,. \quad \text{(A14)}$$

The bispectrum (A13) induces a three-point contribution $(\nu^3/\sigma^3)\xi^{(3)}(\mathbf{x}_1,\mathbf{x}_1,\mathbf{x}_2)$ to the power spectrum of biased tracers which is calculated in [47]. Upon Fourier transformation, it reads as

$$\Delta P_{\rm hh}(k) = 4f_{\rm NL}b_{\rm L}^2\delta_{\rm c}(z)\alpha_M(k)P_\phi(k)\,. \quad \text{(A15)}$$

We follow the steps outlined above to calculate the contribution from the second order trispectrum (A14). After some algebra, the Fourier transform of the four-point correlations of the density field can be written down as

$$\int d^3r\,\xi^{(4)}(\mathbf{x}_1,\mathbf{x}_1,\mathbf{x}_1,\mathbf{x}_2)e^{-i\mathbf{k}\cdot\mathbf{r}} = 8f_{\rm NL}^2\alpha_M(k)P_\phi(k)\int\frac{d^3k_1}{(2\pi)^3}\alpha_M(k_1)P_\phi(k_1)\int\frac{d^3k_2}{(2\pi)^3}\alpha_M(k_2)P_\phi(k_2)\alpha_M\big(|\mathbf{k}+\mathbf{k}_{12}|\big)$$
$$\times\left\{\frac{P_\phi(k_{12})}{P_\phi(k_2)}\left[1+\frac{P_\phi\big(|\mathbf{k}+\mathbf{k}_{12}|\big)}{P_\phi(k)}\right]+\frac{P_\phi\big(|\mathbf{k}+\mathbf{k}_1|\big)}{P_\phi(k)}+\frac{P_\phi\big(|\mathbf{k}+\mathbf{k}_1|\big)}{P_\phi(k_1)}\right.$$
$$\left.+\frac{P_\phi\big(|\mathbf{k}+\mathbf{k}_1|\big)P_\phi\big(|\mathbf{k}+\mathbf{k}_{12}|\big)}{P_\phi(k_1)P_\phi(k_2)}+\frac{P_\phi\big(|\mathbf{k}+\mathbf{k}_1|\big)P_\phi\big(|\mathbf{k}+\mathbf{k}_{12}|\big)}{P_\phi(k)P_\phi(k_2)}\right\} \tag{A16}$$

and

$$\int d^3r\,\xi^{(4)}(\mathbf{x}_1,\mathbf{x}_1,\mathbf{x}_2,\mathbf{x}_2)e^{-i\mathbf{k}\cdot\mathbf{r}} = 4f_{\rm NL}^2\int\frac{d^3k_1}{(2\pi)^3}\alpha_M(k_1)\alpha_M\big(|\mathbf{k}+\mathbf{k}_1|\big)P_\phi(k_1)\int\frac{d^3k_2}{(2\pi)^3}\alpha_M(k_2)\alpha_M\big(|\mathbf{k}+\mathbf{k}_2|\big)P_\phi(k_2)$$
$$\times\left\{P_\phi\big(|\mathbf{k}+\mathbf{k}_{12}|\big)\left[1+2\frac{P_\phi\big(|\mathbf{k}+\mathbf{k}_1|\big)}{P_\phi(k_2)}+\frac{P_\phi\big(|\mathbf{k}+\mathbf{k}_1|\big)P_\phi\big(|\mathbf{k}+\mathbf{k}_2|\big)}{P_\phi(k_1)P_\phi(k_2)}\right]\right.$$
$$+P_\phi(k)\left[1+2\frac{P_\phi\big(|\mathbf{k}+\mathbf{k}_1|\big)}{P_\phi(k_1)}+\frac{P_\phi\big(|\mathbf{k}+\mathbf{k}_1|\big)P_\phi\big(|\mathbf{k}+\mathbf{k}_2|\big)}{P_\phi(k_1)P_\phi(k_2)}\right]$$
$$\left.+2P_\phi\big(|\mathbf{k}+\mathbf{k}_1|\big)\left[\frac{P_\phi(k_{12})}{P_\phi(k_1)}+\frac{P_\phi(k_{12})}{P_\phi(k_2)}\right]\right\}\,. \tag{A17}$$

In the large-scale limit $k\to 0$, these expressions asymptote to

$$\int d^3r\,\xi^{(4)}(\mathbf{x}_1,\mathbf{x}_1,\mathbf{x}_1,\mathbf{x}_2)e^{-i\mathbf{k}\cdot\mathbf{r}} \approx 4f_{\rm NL}^2\,\sigma^4 S_3^{(1)}(M)\alpha_M(k)P_\phi(k)+8f_{\rm NL}^2\alpha_M(k)\int\frac{d^3k_1}{(2\pi)^3}\alpha_M^2(k_1)P_\phi(k_1)$$
$$\times\int\frac{d^3k_2}{(2\pi)^3}\alpha_M^2(k_2)\alpha_M(k_{12})\big[P_\phi(k_1)P_\phi(k_2)+P_\phi(k_1)P_\phi(k_{12})+P_\phi^2(k_{12})\big] \tag{A18}$$
$$\int d^3r\,\xi^{(4)}(\mathbf{x}_1,\mathbf{x}_1,\mathbf{x}_2,\mathbf{x}_2)e^{-i\mathbf{k}\cdot\mathbf{r}} \approx 16f_{\rm NL}^2\sigma^4 P_\phi(k)+16f_{\rm NL}^2\int\frac{d^3k_1}{(2\pi)^3}\,\alpha_M^2(k_1)\int\frac{d^3k_2}{(2\pi)^3}\,\alpha_M^2(k_2)P_\phi(k_2)P_\phi(k_{12})$$
$$\times\big[P_\phi(k_1)+P_\phi(k_2)\big]\,. \tag{A19}$$

Ignoring the second piece in the right-hand side of Eqs (A18) and (A19), the non-Gaussian correction to the halo power spectrum is then easily recast as Eq. (44).

APPENDIX B: SIGNAL-TO-NOISE FOR THE CMB TRISPECTRUM

The formalism for the CMB trispectrum has been established in [29, 30]. The invariance of the 4-point harmonic function of the CMB temperature anisotropy field under the 4! permutations of the coefficients $a_{l_i}^{m_i}$ imposes constraints on the CMB trispectrum $T_{l_3l_4}^{l_1l_2}(L)$ which can be enforced by defining

$$T_{l_3l_4}^{l_1l_2}(L) = P_{l_3l_4}^{l_1l_2}(L)+(2L+1)\sum_{L'}\Bigg[(-1)^{l_2+l_3}$$
$$\times\begin{Bmatrix} l_1 & l_2 & L\\ l_4 & l_3 & L'\end{Bmatrix}P_{l_1l_3}^{l_2l_4}(L')+(-1)^{L+L'}$$
$$\times\begin{Bmatrix} l_1 & l_2 & L\\ l_3 & l_4 & L'\end{Bmatrix}P_{l_1l_4}^{l_3l_2}(L')\Bigg]\,, \tag{B1}$$

where curly brackets are Wigner-6j symbols,

$$P_{l_3l_4}^{l_1l_2}(L) = t_{l_3l_4}^{l_1l_2}(L)+(-1)^{\sum_i l_i}\,t_{l_3l_4}^{l_1l_2}(L)+(-1)^{L+l_3+l_4}$$
$$\times\,t_{l_4l_3}^{l_1l_2}(L)+(-1)^{L+l_1+l_2}t_{l_3l_4}^{l_2l_1}(L)\,, \tag{B2}$$

and the reduced trispectrum $t_{l_3l_4}^{l_1l_2}(L)$ is symmetric under the exchange of its upper and lower indices and fully characterises the model.

The expansion coefficients a_l^m are related to the primordial curvature perturbation $\Phi(\mathbf{k})$ through

$$a_l^m = 4\pi(-i)^l\int\frac{d^3k}{(2\pi)^3}\Phi(\mathbf{k})g_{Tl}(k)Y_l^{m\star}(\hat{\mathbf{k}})\,, \tag{B3}$$

where $g_{Tl}(k)$ is the radiation transfer function. The reduced trispectrum can be calculated from this relation once the four-point function $T_\Phi(\mathbf{k}_1,\mathbf{k}_2,\mathbf{k}_3,\mathbf{k}_4)$ is specified. For a local cubic coupling $g_{\rm NL}\phi^3$,

$$t^{l_1l_2}_{l_3l_4}(L) = \int_0^\infty dr\, r^2 \beta_{l_2}(r)\beta_{l_4}(r) h_{l_1Ll_2} h_{l_3Ll_4} \times \left[\mu_{l_1}(r)\beta_{l_3}(r) + \beta_{l_1}(r)\mu_{l_3}(r)\right] \tag{B4}$$

with

$$\beta_l(r) = \frac{2}{\pi}\int_0^\infty dk\, k^2 P_\phi(k) g_{Tl}(k) j_l(kr) \tag{B5}$$

$$\mu_l(r) = \frac{2}{\pi}\int_0^\infty dk\, k^2 g_{\rm NL} g_{Tl}(k) j_l(kr)\ , \tag{B6}$$

and

$$h_{l_1Ll_2} = \frac{1}{\sqrt{4\pi}}\,\pi_{l_1Ll_2} \begin{pmatrix} l_1 & l_2 & L \\ 0 & 0 & 0 \end{pmatrix}\ . \tag{B7}$$

We also use the notation

$$\pi_{l_1\cdots l_j} = \sqrt{(2l_1+1)\times\cdots\times(2l_j+1)}\ . \tag{B8}$$

Note that most of the contribution to $t^{l_1l_2}_{l_3l_4}(L)$ comes from a small volume centred at the comoving distance $r_\star$ to the surface of last scattering.

The Sachs-Wolfe approximation $g_{Tl}(k) \approx -j_l(kr_\star)/3$ valid at low multipoles $l \ll 100$ provides a useful order-of-magnitude estimate [7, 30, 31, 83]. In this limit, we can approximate $\mu_l(r)$ as $-g_{\rm NL}\delta_D(r-r_\star)/(3r_\star^2)$ since we assume $g_{\rm NL}$ independent of wavenumber. Hence, the reduced trispectrum simplifies to

$$t^{l_1l_2}_{l_3l_4}(L) \approx 9 g_{\rm NL} C^{\rm SW}_{l_2} C^{\rm SW}_{l_4} \left(C^{\rm SW}_{l_1} + C^{\rm SW}_{l_3}\right) h_{l_1Ll_2} h_{l_3Ll_4}\ , \tag{B9}$$

Inserting this expression successively into eqs (B2) and (B1), the CMB trispectrum eventually reads as

$$T^{l_1l_2}_{l_3l_4}(L) = \frac{27}{2\pi} g_{\rm NL}\,(2L+1)\,\pi^2_{l_1l_2l_3l_4} \times \begin{pmatrix} l_1 & l_2 & L \\ 0 & 0 & 0 \end{pmatrix}\begin{pmatrix} l_3 & l_4 & L \\ 0 & 0 & 0 \end{pmatrix} \times \left[C^{\rm SW}_{l_1} C^{\rm SW}_{l_2} C^{\rm SW}_{l_3} + ({\rm cyclic})\right]\ . \tag{B10}$$

where

$$C^{\rm SW}_l = \frac{2}{9\pi}\int_0^\infty dk\, k^2 P_\phi(k) j_l^2(kr_\star) \approx \frac{2\pi A_\phi}{9l(l+1)}\ . \tag{B11}$$

The last equality assumes a nearly scale-invariant spectrum $n_s \approx 1$. The following relation between the Wigner-3j and 6j symbols (e.g., Appendix A of [29]),

$$\sum_{l_3'}(2l_3'+1)(-1)^{\Sigma+l_3'-l_3-m_1-m_1'} \begin{Bmatrix} l_1 & l_2 & l_3 \\ l_1' & l_2' & l_3' \end{Bmatrix} \times \begin{pmatrix} l_2 & l_1' & l_3' \\ m_2 & m_1' & -m_3' \end{pmatrix}\begin{pmatrix} l_1 & l_3' & l_2' \\ m_1 & m_3 & -m_2' \end{pmatrix} = \begin{pmatrix} l_1 & l_2 & l_3 \\ m_1 & m_2 & -m \end{pmatrix}\begin{pmatrix} l_3 & l_1' & l_2' \\ m & m_1' & -m_2' \end{pmatrix} \tag{B12}$$

where $\Sigma = l_1+l_2+l_1'+l_2'$ and the value of m is set by the triangle condition, can be useful to derive Eq.(B10). The signal-to-noise summed up to multipole $l_{\rm max}$, Eq. (36), then becomes

$$\left(\frac{S}{N}\right)^2(<l_{\rm max}) = \left(\frac{27}{2\pi}\right)^2 g^2_{\rm NL} \sum_{l_1>l_2>l_3>l_4}^{l_{\rm max}} \pi^2_{l_1l_2l_3l_4} \times \frac{\left[C^{\rm SW}_{l_1}C^{\rm SW}_{l_2}C^{\rm SW}_{l_3} + ({\rm cyclic})\right]^2}{C^{\rm SW}_{l_1}C^{\rm SW}_{l_2}C^{\rm SW}_{l_3}C^{\rm SW}_{l_4}} \times \sum_{L=0}^{2l_{\rm max}}(2L+1)\begin{pmatrix} l_1 & l_2 & L \\ 0 & 0 & 0 \end{pmatrix}^2\begin{pmatrix} l_3 & l_4 & L \\ 0 & 0 & 0 \end{pmatrix}^2\ . \tag{B13}$$

We can recast the sum over the diagonal modes L into a manifestly symmetric form with the aid of the Gaunt integral

$$\frac{1}{2}\int_{-1}^{+1} dx\, P_{l_1}(x)P_{l_2}(x)P_{l_3}(x) = \begin{pmatrix} l_2 & l_2 & l_3 \\ 0 & 0 & 0 \end{pmatrix}^2 \tag{B14}$$

and the orthogonality relation

$$\sum_{k=0}^{\infty}(2k+1)P_k(x)P_k(y) = 2\delta_D(x-y)\ , \tag{B15}$$

where δ_D is the Dirac delta. We find

$$\sum_{L=0}^{2l_{\rm max}}(2L+1)\begin{pmatrix} l_1 & l_2 & L \\ 0 & 0 & 0 \end{pmatrix}^2\begin{pmatrix} l_3 & l_4 & L \\ 0 & 0 & 0 \end{pmatrix}^2 = \frac{1}{2}\int_{-1}^{+1} dx\, P_{l_1}(x)P_{l_2}(x)P_{l_3}(x)P_{l_4}(x)\ . \tag{B16}$$

There is a strict equality because the Wigner-3j symbols vanish for $L > l_1+l_2$. Eq. (37) for the signal-to-noise then follows by replacing the above equality into Eq.(B13) and summing over all the 4! permutations of the quadruplet (l_1,l_2,l_3,l_4). Although Eq. (37) becomes computationally expensive when $l_{\rm max} \gg 100$ (because we are summing over redundant configurations), we found that it is quite efficient for $l_{\rm max} \lesssim 200$.

Following [31], we can roughly estimate the dependence of the signal-to-noise squared on $l_{\rm max}$ by considering only the contribution of the $L = 1$ mode in Eq.(B13). Consequently, the product of the Wigner-3j symbols squared reduces to $\sim l_1 l_3\, \delta_{l_1-1,l_2}\delta_{l_3-1,l_4}$ and yields $(S/N)^2 \propto l^2_{\rm max}$. However, including all L modes as in Eq. (37) gives a steeper dependence, $(S/N)^2 \propto l^{2.6}_{\rm max}$ (see Fig.9), due to the fact that the Wigner-3j symbols decay slowly with increasing L. This is quite apparent in the classical limit $l_1, l_2, L \gg 1$, where

$$\begin{pmatrix} l_1 & l_2 & L \\ 0 & 0 & 0 \end{pmatrix}^2 \approx \frac{1}{\pi}\left[(l_1+l_2)^2 - L^2\right]^{-1/2}\left[L^2 - (l_1-l_2)^2\right]^{-1/2}\ . \tag{B17}$$

Clearly, the terms in the summation Eq.(B13) decay only as $1/L$ for $L \gg l_1, l_2$. By contrast, the second order contribution to the CMB trispectrum induced by the quadratic coupling $f_{\rm NL}\phi^2$ adds an additional multiplicative factor of $(C_L^{\rm SW})^2$ in the summation over the L modes which increases the relative contribution of the low-L modes (since these now decay as L^{-5}). This is the reason why considering only $L \leq 10$ modes as done in [31] still provides a good approximation to the signal-to-noise of the CMB trispectrum for the $f_{\rm NL}$ model.

[1] V. F. Mukhanov and G. V. Chibisov, Soviet Journal of Experimental and Theoretical Physics Letters **33**, 532 (1981).
[2] A. A. Starobinsky, Physics Letters B **117**, 175 (1982).
[3] S. W. Hawking, Physics Letters B **115**, 295 (1982).
[4] A. H. Guth and S. Pi, Physical Review Letters **49**, 1110 (1982).
[5] T. J. Allen, B. Grinstein, and M. B. Wise, Physics Letters B **197**, 66 (1987).
[6] T. Falk, R. Rangarajan, and M. Srednicki, Phys. Rev. D**46**, 4232 (1992).
[7] A. Gangui, F. Lucchin, S. Matarrese, and S. Mollerach, ApJ**430**, 447 (1994).
[8] N. Bartolo, E. Komatsu, S. Matarrese, and A. Riotto, Phys. Rep. **402**, 103 (2004).
[9] V. Acquaviva, N. Bartolo, S. Matarrese, and A. Riotto, Nuclear Physics B **667**, 119 (2003).
[10] J. Maldacena, Journal of High Energy Physics **5**, 13 (2003).
[11] E. Komatsu, A. Kogut, M. R. Nolta, C. L. Bennett, M. Halpern, G. Hinshaw, N. Jarosik, M. Limon, S. S. Meyer, L. Page, D. N. Spergel, G. S. Tucker, L. Verde, E. Wollack, and E. L. Wright, "Astrophys. J. Supp." **148**, 119 (2003).
[12] P. Creminelli, L. Senatore, M. Zaldarriaga, and M. Tegmark, Journal of Cosmology and Astro-Particle Physics **3**, 5 (2007).
[13] E. Komatsu, J. Dunkley, M. R. Nolta, C. L. Bennett, B. Gold, G. Hinshaw, N. Jarosik, D. Larson, M. Limon, L. Page, D. N. Spergel, M. Halpern, R. S. Hill, A. Kogut, S. S. Meyer, G. S. Tucker, J. L. Weiland, E. Wollack, and E. L. Wright, ApJS **180**, 330 (2009).
[14] K. M. Smith, L. Senatore, and M. Zaldarriaga, ArXiv e-prints (2009).
[15] A. Curto, E. Martínez-González, P. Mukherjee, R. B. Barreiro, F. K. Hansen, M. Liguori, and S. Matarrese, Mon. Not. R. Astron. Soc. **393**, 615 (2009).
[16] D. H. Lyth, C. Ungarelli, and D. Wands, Phys. Rev. D**67**, 023503 (2003).
[17] N. Bartolo, S. Matarrese, and A. Riotto, Phys. Rev. D**69**, 043503 (2004).
[18] K. Enqvist and S. Nurmi, Journal of Cosmology and Astro-Particle Physics **10**, 13 (2005).
[19] K. A. Malik and D. H. Lyth, Journal of Cosmology and Astro-Particle Physics **9**, 8 (2006).
[20] M. Sasaki, J. Väliviita, and D. Wands, Phys. Rev. D**74**, 103003 (2006).
[21] K. Enqvist and T. Takahashi, Journal of Cosmology and Astro-Particle Physics **9**, 12 (2008).
[22] Q.-G. Huang and Y. Wang, Journal of Cosmology and Astro-Particle Physics **9**, 25 (2008).
[23] K. Ichikawa, T. Suyama, T. Takahashi, and M. Yamaguchi, Phys. Rev. D**78**, 023513 (2008).
[24] P. Chingangbam and Q.-G. Huang, Journal of Cosmology and Astro-Particle Physics **4**, 31 (2009).
[25] Q.-G. Huang, Journal of Cosmology and Astro-Particle Physics **11**, 5 (2008).
[26] Q.-G. Huang, Journal of Cosmology and Astro-Particle Physics **6**, 35 (2009).
[27] C. T. Byrnes and G. Tasinato, Journal of Cosmology and Astro-Particle Physics **8**, 16 (2009).
[28] J.-L. Lehners and S. Renaux-Petel, Phys. Rev. D**80**, 063503 (2009).
[29] W. Hu, Phys. Rev. D**64**, 083005 (2001).
[30] T. Okamoto and W. Hu, Phys. Rev. D **66**, 063008 (2002).
[31] N. Kogo and E. Komatsu, Phys. Rev. D **73**, 083007 (2006).
[32] E. Komatsu, ArXiv Astrophysics e-prints (2002).
[33] M. Kunz, A. J. Banday, P. G. Castro, P. G. Ferreira, and K. M. Górski, Astrophys. J. Lett. **563**, L99 (2001).
[34] F. Lucchin and S. Matarrese, ApJ**330**, 535 (1988).
[35] S. Colafrancesco, F. Lucchin, and S. Matarrese, ApJ**345**, 3 (1989).
[36] B. Grinstein and M. B. Wise, ApJ**310**, 19 (1986).
[37] S. Matarrese, F. Lucchin, and S. A. Bonometto, Astrophys. J. Lett. **310**, L21 (1986).
[38] R. Scoccimarro, E. Sefusatti, and M. Zaldarriaga, Phys. Rev. D**69**, 103513 (2004).
[39] E. Sefusatti and E. Komatsu, Phys. Rev. D**76**, 083004 (2007).
[40] E. Sefusatti, ArXiv e-prints (2009).
[41] D. Jeong and E. Komatsu, ArXiv e-prints (2009).
[42] M. Kamionkowski, L. Verde, and R. Jimenez, Journal of Cosmology and Astro-Particle Physics **1**, 10 (2009).
[43] T. Y. Lam and R. K. Sheth, Mon. Not. R. Astron. Soc. **395**, 1743 (2009).
[44] C. Hikage, E. Komatsu, and T. Matsubara, ApJ**653**, 11 (2006).
[45] C. Hikage, P. Coles, M. Grossi, L. Moscardini, K. Dolag, E. Branchini, and S. Matarrese, Mon. Not. R. Astron. Soc. **385**, 1613 (2008).
[46] N. Dalal, O. Doré, D. Huterer, and A. Shirokov, Phys. Rev. D**77**, 123514 (2008).
[47] S. Matarrese and L. Verde, Astrophys. J. Lett. **677**, L77 (2008).
[48] A. Slosar, C. Hirata, U. Seljak, S. Ho, and N. Padmanabhan, Journal of Cosmology and Astro-Particle Physics **8**, 31 (2008).
[49] N. Afshordi and A. J. Tolley, Phys. Rev. D**78**, 123507 (2008).
[50] C. Carbone, L. Verde, and S. Matarrese, Astrophys. J. Lett. **684**, L1 (2008).
[51] U. Seljak, Physical Review Letters **102**, 021302 (2009).
[52] E. Sefusatti, M. Liguori, A. P. S. Yadav, M. G. Jackson, and E. Pajer, ArXiv e-prints (2009).
[53] V. Desjacques, U. Seljak, and I. T. Iliev, Mon. Not. R. Astron. Soc. **396**, 85 (2009).
[54] A. Pillepich, C. Porciani, and O. Hahn, ArXiv e-prints

(2008).
[55] M. Grossi, L. Verde, C. Carbone, K. Dolag, E. Branchini, F. Iannuzzi, S. Matarrese, and L. Moscardini, ArXiv e-prints (2009).
[56] U. Seljak and M. Zaldarriaga, ApJ**469**, 437 (1996).
[57] V. Springel, Mon. Not. R. Astron. Soc. **364**, 1105 (2005).
[58] Y. B. Zel'Dovich, A&A **5**, 84 (1970).
[59] J. N. Fry, ApJ**279**, 499 (1984).
[60] M. H. Goroff, B. Grinstein, S.-J. Rey, and M. B. Wise, ApJ**311**, 6 (1986).
[61] F. R. Bouchet, R. Juszkiewicz, S. Colombi, and R. Pellat, Astrophys. J. Lett. **394**, L5 (1992).
[62] F. Bernardeau, ApJ**433**, 1 (1994).
[63] R. Scoccimarro, Mon. Not. R. Astron. Soc. **299**, 1097 (1998).
[64] P. McDonald, Phys. Rev. D**78**, 123519 (2008).
[65] S. R. Knollmann and A. Knebe, ArXiv e-prints (2009).
[66] S. P. D. Gill, A. Knebe, and B. K. Gibson, Mon. Not. R. Astron. Soc. **351**, 399 (2004).
[67] M. S. Warren, P. J. Quinn, J. K. Salmon, and W. H. Zurek, ApJ**399**, 405 (1992).
[68] C. Lacey and S. Cole, Mon. Not. R. Astron. Soc. **271**, 676 (1994).
[69] V. R. Eke, S. Cole, and C. S. Frenk, Mon. Not. R. Astron. Soc. **282**, 263 (1996).
[70] G. L. Bryan and M. L. Norman, ApJ**495**, 80 (1998).
[71] W. H. Press and P. Schechter, ApJ**187**, 425 (1974).
[72] J. R. Bond, S. Cole, G. Efstathiou, and N. Kaiser, ApJ**379**, 440 (1991).
[73] M. Lo Verde, A. Miller, S. Shandera, and L. Verde, Journal of Cosmology and Astro-Particle Physics **4**, 14 (2008).
[74] S. Matarrese, L. Verde, and R. Jimenez, ApJ**541**, 10 (2000).
[75] M. Grossi, K. Dolag, E. Branchini, S. Matarrese, and L. Moscardini, Mon. Not. R. Astron. Soc. **382**, 1261 (2007).
[76] R. K. Sheth and G. Tormen, Mon. Not. R. Astron. Soc. **308**, 119 (1999).
[77] P. Valageas, ArXiv e-prints (2009).
[78] T. Y. Lam and R. K. Sheth, ArXiv e-prints (2009).
[79] T. Y. Lam, R. K. Sheth, and V. Desjacques, Mon. Not. R. Astron. Soc. **399**, 1482 (2009).
[80] A. Slosar, Journal of Cosmology and Astro-Particle Physics **3**, 4 (2009).
[81] U. Seljak, N. Hamaus, and V. Desjacques, Physical Review Letters **103**, 091303 (2009).
[82] P. McDonald and U. Seljak, ArXiv e-prints (2008).
[83] E. Komatsu and D. N. Spergel, Phys. Rev. D**63**, 063002 (2001).
[84] M. Grossi, E. Branchini, K. Dolag, S. Matarrese, and L. Moscardini, Mon. Not. R. Astron. Soc. **390**, 438 (2008).
[85] A. Taruya, K. Koyama, and T. Matsubara, Phys. Rev. D**78**, 123534 (2008).
[86] X. Kang, P. Norberg, and J. Silk, Mon. Not. R. Astron. Soc. **376**, 343 (2007).
[87] R. K. Sheth and G. Tormen, Mon. Not. R. Astron. Soc. **329**, 61 (2002).
[88] M. Maggiore and A. Riotto, ArXiv e-prints (2009).
[89] Z. Lukić, D. Reed, S. Habib, and K. Heitmann, ApJ**692**, 217 (2009).
[90] L. Boubekeur and D. H. Lyth, Phys. Rev. D**73**, 021301 (2006).
[91] C. T. Byrnes, M. Sasaki, and D. Wands, Phys. Rev. D**74**, 123519 (2006).
[92] M.-X. Huang and G. Shiu, Phys. Rev. D**74**, 121301 (2006).